DOI: 10.1002/ejic.200900848

Structural, Spectroscopic, and Proton-Coupled Electron-transfer Behavior of Pyrazolyl-3,5-bis(benzimidazole)-Bridged Homo- and Heterochiral $Ru^{II}Ru^{II}$, $Os^{II}Os^{II}$, and $Os^{II}Ru^{II}$ 2,2′-Bipyridine Complexes

Sujoy Baitalik,*[a,b] Supriya Dutta,[a] Papu Biswas,[a,c] Ulrich Flörke,[d] Eberhard Bothe,[e] and Kamalaksha Nag*[a]

Keywords: Ruthenium / Osmium / Electrochemistry / Electron transfer / Bridging ligands

The homo- and heterobimetallic complexes $[(bpy)_2M^{II}(H_2pzbzim)M'^{II}(bpy)_2](ClO_4)_3\cdot nH_2O$ (**1**, **3**, **5**) and their corresponding deprotonated complexes $[(bpy)_2M^{II}(pzbzim)M'^{II}(bpy)_2](ClO_4)\cdot nH_2O$ (**2**, **4**, **6**) [where M^{II}, M'^{II} = Ru (**1**, **2**) = Os (**3**, **4**); M^{II} = Os and M'^{II} = Ru (**3**, **5**); bpy = 2,2′-bipyridine; H_3pzbzim = pyrazole-3,5-bis(benzimidazole)] were synthesized, separated to their heterochiral (**a**, ΛΔ/ΔΛ) and homochiral (**b**, ΛΛ/ΔΔ) diastereoisomers, and characterized by elemental analyses, ESI-MS, and ^{1}H NMR spectroscopy. The X-ray structures of **1a**, **3a**, and **5a** show the involvement of two pyridine rings of two bpy ligands in strong intramolecular nonbonded π–π interaction. The occurrence of a C–H···π interaction between an aromatic C–H and the π-cloud of a pyridine ring leads to strong electronic shielding of this proton (^{1}H NMR). In all cases, the two diastereoisomers show practically no differences in their absorption spectra, redox potentials, and pK values. The large shifts in the $E_{1/2}$ values to less positive potentials and substantial redshifts in the MLCT bands that occur on deprotonation of **1**, **3**, and **5** are energetically correlated. From the profiles of $E_{1/2}$(1), (2) vs. pH over the pH range 1–12, the equilibrium constants and standard redox potentials for all the complex species in the metal oxidation states II·II, II·III, and III·III and the bridged ligand in the protonation states H_2pzbzim$^-$, Hpzbzim^{2-}, and pzbzim^{3-} have been evaluated. Using these values the bond dissociation free energies for the benzimidazole N–H bonds have been estimated. Spectroelectrochemical studies have been carried out for **1a**, **3a**, and **5a** in the range 400–1100 nm. With stepwise oxidation of the metal centers replacement of MLCT bands by LMCT bands occur gradually with the observation of sharp isosbestic points. In the case of **1a**, a band observed at λ_{max} = 910 nm for the $Ru^{II}Ru^{III}$ species has been ascribed to intervalence charge transfer (IVCT) transition.

Introduction

Ruthenium(II) and osmium(II) polypyridine complexes are considered as iconic building blocks for designing photomolecular devices because of a unique combination of their photophysical and redox properties.[1–5] The efficiency of photoinduced energy/or electron-transfer processes in dyads is strongly regulated by bridging ligands that connect the donor and acceptor units.[6–9] Generally, bridging ligands are either electron-rich or electron-poor. With electron-poor bridging ligands such as oligopyridine/pyrazine/pyrimidine etc., metal–metal interactions occur through lowest unoccupied molecular orbitals (LUMO) of the bridge. On the other hand, highest occupied molecular orbitals (HOMO) of electron-rich bridging ligands are involved in intermetallic interactions. Typically, bridging ligands of this sort contain proton dissociable azoles, such as triazole, pyrazole, benzimidazole, etc.[10,11] The synthesis of homo-/or heterobimetallic ruthenium(II) and osmium(II) complexes with bidentate chelating units are almost invariably associated with the formation of homochiral (ΛΛ/ΔΔ) and heterochiral (ΛΔ/ΔΛ) diastereoisomers. All earlier physicochemical studies reported in the literature were made with mixtures of diastereoisomers. However, now it has become customary to separate the diastereoisomers[12–15] prior to physicochemical study.

The absorption spectral features of dinuclear ruthenium(II) and osmium(II) complexes are dominated by charge-transfer transitions involving metal-to-ligand (MLCT), ligand-to-metal (LMCT), metal-to-metal (MMCT), and intervalence (IVCT) bands in addition to intraligand transitions. Analysis of IVCT transitions in

[a] Department of Inorganic Chemistry, Indian Association for the Cultivation of Science
Jadavpur, Kolkata 700032, India
Fax: +91-33-2473-2805
E-mail: ickn@iacs.res.in
[b] Department of Chemistry, Inorganic Chemistry Section, Jadavpur University
Jadavpur, Kolkata 700032, India
[c] Department of Chemistry, Bengal Engineering and Science University
Shibpur, Howrah 711103, India
[d] Department of Inorganic and Analytical Chemistry, University of Paderborn
33098, Paderborn, Germany
[e] Max Planck Institute for Bioinorganic Chemistry,
Stiftstr. 34–36, 45470, Mülheim, Germany

Supporting information for this article is available on the WWW under http://dx.doi.org/10.1002/ejic.200900848.

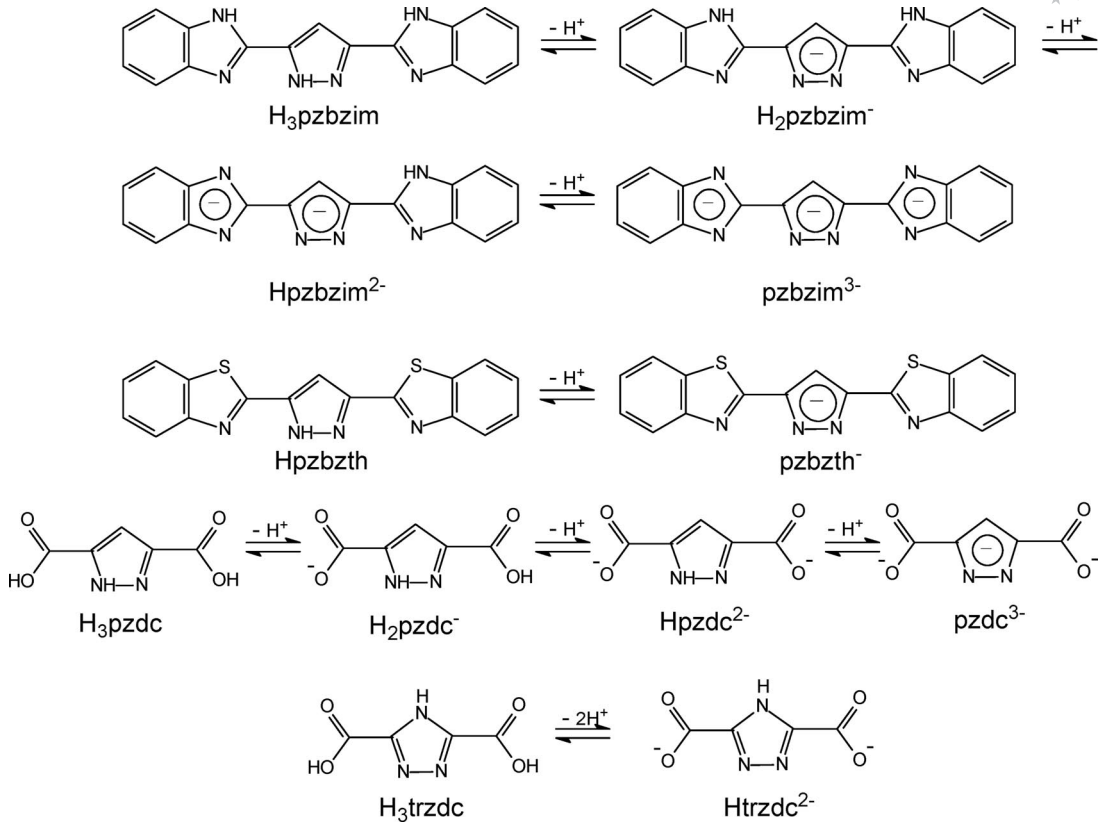

Scheme 1.

mixed-valence ($M^{II}M^{III}$) ruthenium and osmium complexes provide useful information regarding the extent of electronic coupling between the metal centers that can range between valence-localized to valence-delocalized states.[16–21] In the context of mixed-valence state, evaluation of the comproportionation constant (K_c) is of considerable interest.[22–24] Spectroelectrochemical study provides a convenient way to follow the evolution and disappearance of different charge-transfer transitions as the oxidation states of the metal ions change from $M^{II}M^{II}$ to $M^{II}M^{III}$ to $M^{III}M^{III}$.

Proton-coupled electron-transfer reactions,[25,26] which can take place either in a concerted way or in stepwise manner, are of considerable interest in azole-bridged ruthenium(II) and osmium(II) complexes because they can be subjected to both proton- and electron-transfer reactions. Significant changes in redox potentials, absorbances, and luminescence properties of such complexes can be brought about by subjecting to protonation–deprotonation equilibrium. Indeed, depending upon the extent of perturbation of these properties, proton-driven molecular switches can be developed.[27–29]

We have reported earlier[30] the synthesis, structure, stereochemistry, and electrochemistry of mononuclear and dinuclear ruthenium(II) and osmium(II) polypyridine complexes in combination with the bridging ligands pyrazole-3,5-bis(benzimidazole), H_3pzbzim;[30a,30c] pyrazole-3,5-bis(benzothiazole), Hpzbzth;[30b] pyrazole-3,5-dicarboxylic acid, H_3pzdc;[30d,30f] and triazole-3,5-dicarboxylic acid, H_3trzdc[30e] (Scheme 1). The present study is concerned with the chemistry of homochiral (ΛΛ/ΔΔ) and heterochiral (ΛΔ/ΔΛ) diastereoisomers of RuRu, OsOs, and OsRu complexes $[(bpy)_2M^{II}(H_2pzbzim)M'^{II}(bpy)_2](ClO_4)_3{\cdot}nH_2O$ and $[(bpy)_2M^{II}(pzbzim)M'^{II}(bpy)_2](ClO_4){\cdot}nH_2O$, where M/M′ = Ru/Os and bpy = 2,2′-bipyridine. Of particular interest to us has been the examination of the role of chirality on the structural, redox behavior, and spectroscopic characteristics of the compounds. It has also been of interest to follow the trends in proton-coupled electron-transfer reactions along the series RuRu, OsOs, and OsRu, as the bridged-ligand $H_2pzbzim^-$ successively gets dissociated to $Hpzbzim^{2-}$ and $pzbzim^{3-}$, while the oxidation states of the metal centers change from $M^{II}M^{II}$ to $M^{II}M^{III}$ to $M^{III}M^{III}$. Further, the sequential changes that occur in the absorption spectra of the complexes with the stepwise oxidation of the metal centers have been followed by spectroelectrochemical measurements.

Results and Discussion

Synthesis

We have reported earlier[30a] the preparation and separation of *meso* (ΛΔ) and *rac* (ΛΛ/ΔΔ) forms of the diruthenium(II) complexes $[(bpy)_2Ru(H_2pzbzim)Ru(bpy)_2](ClO_4)_3{\cdot}5H_2O$ (**1a/1b**) and $[(bpy)_2Ru(pzbzim)Ru(bpy)_2](ClO_4){\cdot}3H_2O$ (**2a/2b**). The diosmium(II) complex $[(bpy)_2Os(H_2pzbzim)Os(bpy)_2](ClO_4)_3{\cdot}2H_2O$ (**3**) has been obtained as a mixture

(ca. 1:1) of heterochiral and homochiral diastereoisomers by treating a mixture of *cis*-$[Os(bpy)_2Cl_2]$, $H_3pzbzim$, and $N(C_2H_5)_3$ in a 2:1:1 molar ratio in boiling ethanol/water (1:1) for 72 h. Separation of the *meso* (ΛΔ, **3a**) and *rac* (ΛΛ/ΔΔ, **3b**) forms was achieved by fractional crystallization from methanol/acetonitrile (2:1), in which **3b** is more soluble than **3a**. The *meso* (**4a**) and *rac* (**4b**) forms of $[(bpy)_2Os(pzbzim)Os(bpy)_2](ClO_4)\cdot 2H_2O$ (**4**) were obtained by quantitative deprotonation of **3a** and **3b**, respectively, with sodium methoxide. The heterobimetallic complex $[(bpy)_2Os(H_2pzbzim)Ru(bpy)_2](ClO_4)_3\cdot 4H_2O$ (**5**) was produced as a mixture (ca. 1:1) of heterochiral (ΛΔ/ΔΛ) and homochiral (ΛΛ/ΔΔ) diastereoisomers by treating equimolar amounts of $[(bpy)_2Ru(C_2H_5OH)_2]^{2+}$, $[(bpy)_2Os(H_3pzbzim)](ClO_4)_2\cdot 2H_2O$, and $N(C_2H_5)_3$ in ethanol at its boiling temperature for 24 h. The alternative reaction involving $[(bpy)_2Ru(H_3pzbzim)](ClO_4)_2\cdot 2H_2O$, *cis*-$[Os(bpy)_2Cl_2]$, and $N(C_2H_5)_3$ turned out to be far-less efficient. The enantiomeric pairs ΛΔ/ΔΛ (**5a**) and ΛΛ/ΔΔ (**5b**), again, were separated by fractional crystallization from methanol/acetonitrile, taking advantage of the lesser solubility of **5a** in the solvent. Similar to **4a** and **4b**, the deprotonated heterochiral (ΛΔ/ΔΛ, **6a**) and homochiral (ΛΛ/ΔΔ, **6b**) diastereoisomers of $[(bpy)_2Os(pzbzim)Ru(bpy)_2](ClO_4)\cdot 3H_2O$ (**6**) were obtained by treating **5a** and **5b**, respectively, with two equivalents of sodium methoxide.

All of the compounds were characterized by their elemental (C, H, and N) and mass spectral (ESI-MS) analyses. The ESI-MS of the heterodinuclear compound $[(bpy)_2Os(H_2pzbzim)Ru(bpy)_2](ClO_4)_3\cdot 4H_2O$ (**5**) was of particular interest, because, as will be seen, the X-ray structure determination of **5a** revealed that the two metal centers in this compound are positionally disordered over two sites with equal occupancy. That the observed structure of **5a** is not due to an alternative possibility of static disordering of homodinuclear $Os^{II}Os^{II}$ and $Ru^{II}Ru^{II}$ species has been established by its mass spectra. The ESI-MS of **5a** in acetonitrile (Figure S1, Supporting Information) shows two strong clusters of peaks with m/z = 405.1 and 607.2, which correspond to those of $[(bpy)_2Os(H_2pzbzim)Ru(bpy)_2]^{3+}$ and $[(bpy)_2Os(Hpzbzim)Ru(bpy)_2]^{2+}$, respectively. The excellent agreement between the observed and simulated isotopic distribution patterns of the peaks clearly indicates that **5** is a genuine heterobimetallic $Os^{II}Ru^{II}$ compound.

Crystal Structures of *meso* (ΛΔ) $[(bpy)_2Os^{II}(H_2pzbzim)Os^{II}(bpy)_2](ClO_4)_3\cdot 2H_2O$ (3a) and Heterochiral (ΛΔ/ΔΛ) $[(bpy)_2Os^{II}(H_2pzbzim)Ru^{II}(bpy)_2](ClO_4)_3\cdot 4H_2O$ (5a)

It should be mentioned at the outset that diffraction-quality crystals could be obtained only for the less-soluble diastereoisomers (**1a**, **3a**, and **5a**) of $[(bpy)_2M^{II}(H_2pzbzim)M'^{II}(bpy)_2](ClO_4)_3\cdot nH_2O$ compounds. Despite many attempts, discrete crystals of **1b**, **3b**, and **5b** suitable for structure determination could not be isolated. Both **1a** and **5a** crystallize in monoclinic form with the space group $P2_1/c$, while **3a** is triclinic with the space group $P\bar{1}$. The structure of *meso* $[(bpy)_2Ru^{II}(H_2pzbzim)Ru^{II}(bpy)_2](ClO_4)_3\cdot 5H_2O$ (**1a**) was reported previously.[30a] However, some of its structural aspects that are relevant to this study and were not considered earlier will be discussed here.

A capped stick projection of cation $\mathbf{3a}^{3+}$ and an ORTEP view of cation $\mathbf{5a}^{3+}$ are shown in Figures 1 and 2, respectively. Selected bond lengths and angles for **3a** and **5a** are listed in Tables 1 and 2. As may be noted, both $\mathbf{3a}^{3+}$ and $\mathbf{5a}^{3+}$ are heterochiral. In terms of chirality descriptor, homodinuclear $\mathbf{3a}^{3+}$ is the *meso* (ΛΔ) form, while heterodinuclear $\mathbf{5a}^{3+}$ is a ΛΔ/ΔΛ enantiomeric pair. The metal centers in $\mathbf{5a}^{3+}$ are disordered over two sites M1 and M2 with almost equal occupancy (0.51 Ru/ 0.49 Os for M1 and 0.49 Ru/0.51 Os for M2). As has been established by ESI-MS, **5a** is not a 1:1 stoichiometric combination of the homodinuclear $Os^{II}Os^{II}$ and $Ru^{II}Ru^{II}$ compounds, and thus, the possibility of static disordering is ruled out.

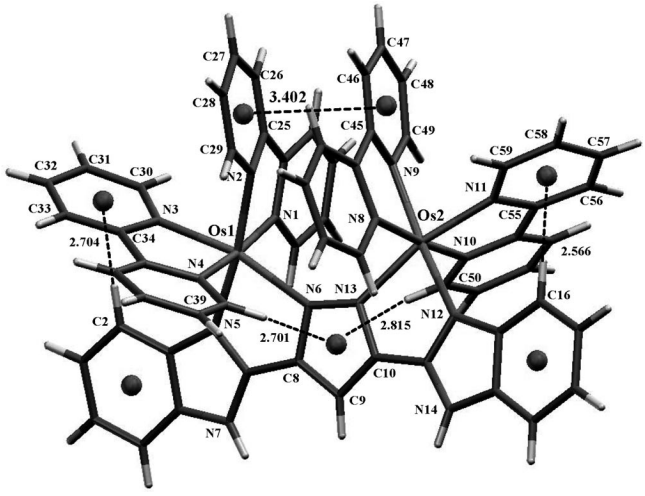

Figure 1. Capped stick projection of *meso* $[(bpy)_2Os(H_2pzbzim)Os(bpy)_2]^{3+}$ ($\mathbf{3a}^{3+}$) showing π–π and CH–π interactions.

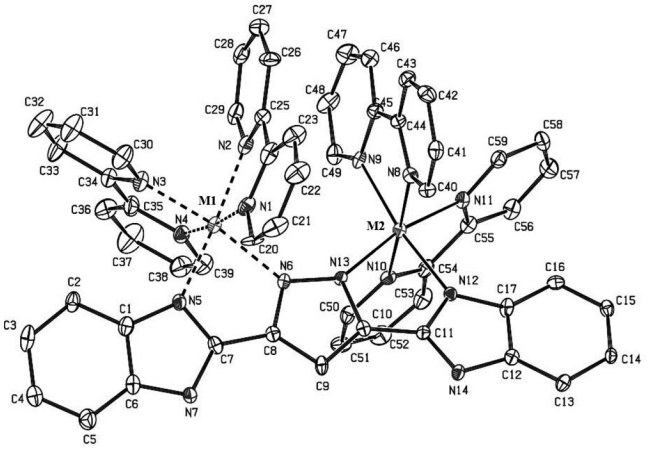

Figure 2. ORTEP representation of $[(bpy)_2Os(H_2pzbzim)Ru(bpy)_2]^{3+}$ ($\mathbf{5a}^{3+}$) showing 30% probability ellipsoid plots. Hydrogen atoms are omitted for clarity.

Table 1. Selected bond lengths/Å and angles/° for *meso* (ΛΔ) [$(bpy)_2$-$Os(H_2pzbzim)Os(bpy)_2$]$(ClO_4)_3$·$2H_2O$ (**3a**).

Os1–N1	2.040 (6)	Os2–N8	2.023 (6)
Os1–N2	2.057 (5)	Os2–N9	2.053 (5)
Os1–N3	2.039 (5)	Os2–N10	2.037 (5)
Os1–N4	2.046 (6)	Os2–N11	2.041 (5)
Os1–N5	2.081 (5)	Os2–N12	2.082 (5)
Os1–N6	2.141 (5)	Os2–N13	2.110 (5)
Os1···Os2	4.625 (6)		
N1–Os1–N2	78.5 (2)	N8–Os2–N9	78.5 (2)
N1–Os1–N3	99.6 (2)	N8–Os2–N10	174.8 (2)
N1–Os1–N4	172.9 (2)	N8–Os2–N11	100.3 (2)
N1–Os1–N5	98.0 (2)	N8–Os2–N12	96.8 (2)
N1–Os1–N6	91.0 (2)	N8–Os2–N13	89.2 (2)
N2–Os1–N3	80.4 (2)	N9–Os2–N10	96.3 (2)
N2–Os1–N4	94.5 (2)	N9–Os2–N11	82.6 (19)
N2–Os1–N5	171.0 (2)	N9–Os2–N12	172.0 (2)
N2–Os1–N6	111.2 (2)	N9–Os2–N13	108.8 (2)
N3–Os1–N4	78.4 (2)	N10–Os2–N11	78.4 (2)
N3–Os1–N5	92.2 (2)	N10–Os2–N12	88.3 (2)
N3–Os1–N6	165.8 (2)	N10–Os2–N13	93.0 (2)
N4–Os1–N5	88.9 (2)	N11–Os2–N12	91.8 (2)
N4–Os1–N6	92.1 (2)	N11–Os2–N13	166.5 (2)
N5–Os1–N6	76.9 (2)	N12–Os2–N13	77.5 (2)

Table 2. Selected bond lengths/Å and angles/° for heterochiral (ΛΔ/ΔΛ) [$(bpy)_2Os(H_2pzbzim)Ru(bpy)_2$]$(ClO_4)_3$·$4H_2O$ (**5a**).

M1–N1	2.060 (9)	M2–N8	2.043 (8)
M1–N2	2.056 (10)	M2–N9	2.051 (9)
M1–N3	2.043 (9)	M2–N10	2.049 (8)
M1–N4	2.036 (9)	M2–N11	2.038 (8)
M1–N5	2.076 (9)	M2–N12	2.082 (8)
M1–N6	2.137 (8)	M2–N13	2.131 (8)
M1···M2	4.665 (3)		
N1–M1–N2	78.5 (4)	N8–M2–N9	78.3 (3)
N1–M1–N3	96.8 (4)	N8–M2–N10	173.8 (4)
N1–M1–N4	173.9 (4)	N8–M2–N11	97.3 (3)
N1–M1–N5	97.3 (4)	N8–M2–N12	96.2 (3)
N1–M1–N6	86.5 (3)	N8–M2–N13	90.9 (3)
N2–M1–N3	81.9 (4)	N9–M2–N10	96.1 (3)
N2–M1–N4	96.0 (4)	N9–M2–N11	82.0 (3)
N2–M1–N5	174.0 (4)	N9–M2–N12	171.6 (3)
N2–M1–N6	106.5 (3)	N9–M2–N13	108.1 (3)
N3–M1–N4	79.6 (4)	N10–M2–N11	79.0 (4)
N3–M1–N5	94.4 (4)	N10–M2–N12	88.9 (3)
N3–M1–N6	171.4 (4)	N10–M2–N13	93.5 (3)
N4–M1–N5	88.0 (4)	N11–M2–N12	92.4 (3)
N4–M1–N6	97.8 ()	N11–M2–N13	168.2 (3)
N5–M1–N6	77.3 (3)	N12–M2–N13	78.2 (3)

In $\mathbf{3a}^{3+}$ and $\mathbf{5a}^{3+}$, the two $M^{II}(bpy)_2$ units are bridged by the pyrazolate nitrogen atoms N6 and N13 of $H_2pzbzim^-$, while its benzimidazole nitrogen atoms N5 and N12 provide the sixth coordination site to the two metal centers. The equatorial planes of the two distorted octahedra are constituted by the atoms N2, N3, N5, N6 and N9, N11, N12, N13. The two pyridyl nitrogen atoms of each bpy ligand are coordinated alternatively in axial and equatorial modes.

In all three compounds, three types of metal–nitrogen distances are observed. The longest M–N distances involve the pyrazolate nitrogen atoms with average values of 2.149(14) Å for **1a**, 2.125(15) Å for **3a**, and 2.134(3) Å for **5a**. The next longest M–N distances pertain to the benzimidazole nitrogen atoms, whose average values are 2.092(13) Å for **1a**, 2.081(1) Å for **3a**, and 2.079(3) Å for **5a**. The bpy ligands provide the shortest M–N distances with average values of 2.057(11) Å for **1a**, 2.042(9) Å for **3a**, and 2.047(12) Å for **5a**. All M–N distances decrease in the order **1a** (Ru^{II} Ru^{II}) > **5a** (Os^{II} Ru^{II}) > **3a** (Os^{II} Os^{II}), although the differences across the series are small. The deviations in the metal centers from idealized octahedral geometry can be gauged by considering the ranges of the *trans* angles, which lie between 166 and 175°. There are some subtle structural differences of $\mathbf{3a}^{3+}$ from $\mathbf{1a}^{3+}$ and $\mathbf{5a}^{3+}$, which are isotypes. This becomes evident if the dihedral angles between the planes of the pyridyl rings of each bpy ligand of the compounds are considered. Thus, designating each pyridine ring by the number of its nitrogen atom, the following interplanar angles are obtained:

$\mathbf{1a}^{3+}$: 13.67 (1/2), 2.73 (3/4), 15.31 (8/9), 3.25° (10/11)

$\mathbf{3a}^{3+}$: 16.76 (1/2), 11.07 (3/4), 15.64 (8/9), 12.01° (10/11)

$\mathbf{5a}^{3+}$: 13.38 (1/2), 3.37 (3/4), 13.76 (8/9), 3.89° (10/11).

It may be noted that in both $\mathbf{1a}^{3+}$ and $\mathbf{5a}^{3+}$, two bpy ligands are almost coplanar, while the other two bpy ligands deviate considerably from coplanarity. In contrast, all four bpy ligands in $\mathbf{3a}^{3+}$ deviate significantly from coplanarity.

Two other important structural features, viz. the occurrence of aromatic π–π and CH–π interactions deserve consideration. As may be noted in the capped stick representation of $\mathbf{3a}^{3+}$ (Figure 1), the pyridine ring coordinated to Os1 by N2 is in face-to-face alignment with the pyridine ring that is coordinated to Os2 by N9. The centroid–centroid distance between these two rings is 3.402 Å, while the dihedral angle between the ring planes is 1.5°. Clearly, the two heteroaromatic rings (2/9) are involved in strong π–π interactions. The same interactions in $\mathbf{1a}^{3+}$ and $\mathbf{5a}^{3+}$ (Figure S2a,b; Supporting Information) have the following values for centroid–centroid distance and dihedral angles: 3.593 Å and 8.2° for $\mathbf{1a}^{3+}$, 3.526 Å and 7.9° for $\mathbf{5a}^{3+}$. In $\mathbf{3a}^{3+}$, the π–π distance is shortest and the dihedral angle is lowest. It may be mentioned that perfect or near-perfect face-to-face alignment of ring planes occurs rarely.[31,32] More usual are the cases of slipped-type π–π interaction, where the ring planes are displaced in a parallel fashion. To be reckoned as π–π interacting, the distance between the centroids of the two rings and the angle between the vector of ring centroids and the ring normal should be within 3.8 Å and 20°, respectively.[31–33] It is important to note that the molecular models of the homochiral diastereoisomers, however, indicate the absence of similar π–π interaction.

The fact that crystals suitable for structure determination could be obtained for **1a**, **3a**, and **5a** but not for **1b**, **3b**, or **5b** raises the question whether this is due to the presence and absence of π–π interactions, respectively. To obtain a better understanding, a few more related structures reported previously by us[30] have been reexamined in this light. Thus, for $[(bpy)_2Ru^{II}(pzbzth)Ru^{II}(bpy)_2](ClO_4)_3$·$H_2O$,[30b] the structure could be determined only for the *meso* form. Figure S3 (Supporting Information) shows that here also a π–π interaction occurs between two pyridine rings. Again, for the $Ru^{II}Ru^{II}$, $Os^{II}Os^{II}$, and $Os^{II}Ru^{II}$ [$(bpy)_2$-

Table 3. Metrical parameters involving intramolecular π–π and CH–π interactions[a] and metal–metal distances in homochiral and heterochiral $Ru^{II}Ru^{II}$, $Os^{II}Os^{II}$, and $Os^{II}Ru^{II}$ compounds.

Compound	Chirality	π–π Interaction		CH–π Interaction		$M^{II}\cdots M^{II}$
		Distance / Å	Angle / °	Distance / Å	Angle / °	Distance / Å
1a ($Ru^{II}Ru^{II}$)	*meso* (ΛΔ)	3.593	8.2	2.704	158.9	4.717
				2.691	154.7	
				2.606	139.4	
3a ($Os^{II}Os^{II}$)	*meso* (ΛΔ)	3.402	1.5	2.704	144.3	4.625
				2.566	150.2	
				2.701	139.8	
				2.815	136.1	
5a ($Os^{II}Ru^{II}$)	heterochiral (ΛΔ/ΔΛ)	3.526	7.9	2.689	160.6	4.665
				2.653	153.2	
				2.761	139.8	
$[(bpy)_2Ru^{II}(pzbzth)Ru^{II}(bpy)_2](ClO_4)_3\cdot H_2O$	*meso* (ΛΔ)	3.609	10.3	2.603	147.7	4.723
				2.544	168.1	
				2.766	139.0	
$[(bpy)_2M^{II}(pzdc)M'^{II}(bpy)_2](ClO_4)\cdot H_2O$						
$Ru^{II}Ru^{II}$	*rac* (ΛΛ/ΔΔ)	3.382	4.9	2.984	135.3	4.685
				2.953	139.1	
$Os^{II}Os^{II}$	*rac* (ΛΛ/ΔΔ)	3.371	6.0	3.016	132.8	4.662
				2.982	117.9	
$Os^{II}Ru^{II}$	homochiral (ΛΛ/ΔΔ)	3.377	5.3	3.018	133.3	
				2.937	139.6	4.690

[a] For the connectivities in the concerned interactions see: Figure 1 for **3a**; Figure S2a,b for **1a** and **5a**; Figure S3 for *meso* $[(bpy)_2$-RuII(pzbzth)RuII$(bpy)_2](ClO_4)_3\cdot H_2O$; Figure S4a–c for homochiral $[(bpy)_2$MII(pzdc)M′II$(bpy)_2](ClO_4)\cdot H_2O$.

$M^{II}(pzdc)M'^{II}(bpy)_2](ClO_4)\cdot H_2O$[30d,30f] complexes, the structures could be determined only for the homochiral diastereoisomers. As shown in Figure S4a–c (Supporting Information), in these cases also a strong intramolecular π–π interaction occurs between two pyridine rings. Indeed, the distances between the centroids of the rings are quite short. Taken together, these observations indicate that intramolecular π–π interaction plays a definitive role to stabilize the crystal system of that particular diastereoisomers where this interaction occurs.

The occurrence of intramolecular CH–π interactions in $\mathbf{3a}^{3+}$, $\mathbf{1a}^{3+}$, and $\mathbf{5a}^{3+}$ are shown in Figures 1 and S2a,b (Supporting Information), respectively. In $\mathbf{3a}^{3+}$, the hydrogen atoms H2 and H16 of the two phenyl rings are in close proximity to the centers of the pyridyl rings with the N3 and N11 nitrogen atoms, respectively. The distances of H2 and H16 from the centroids of the two pyridyl rings are 2.704 and 2.566 Å, respectively, while the angles C2–H2···π (centroid of the N3–C30···C34 ring) and C16–H16···π (centroid of the N11–C55···C59 ring) are 144.3 and 150.2°, respectively. The implication of these point-to-face or edge-on CH–π interactions[34,35] on the ^{1}H NMR spectra of the compounds will be seen later. Further, the H39 and H50 hydrogen atoms of the pyridyl rings C35···C39–N4 and C50···C54–N10 are close to the center of the pyrazolate ring π cloud and corresponding distances and angles are 2.701 and 2.815 Å and 139.8 and 136.1°. Similar interactions that occur with $\mathbf{1a}^{3+}$ and $\mathbf{5a}^{3+}$ can be seen in Figure S2a,b (Supporting Information) and the metrical parameters involved therein are listed in Table 3.

The CH–π interactions occur also with *meso* $[(bpy)_2Ru^{II}$-$(pzbzth)Ru^{II}(bpy)_2]^{3+}$ (see Figure S3 for connectivities, Supporting Information) and the homochiral diastereoisomers of the $Ru^{II}Ru^{II}$, $Os^{II}Os^{II}$, and $Os^{II}Ru^{II}$ complexes $[(bpy)_2$-$M^{II}(pzdc)M'^{II}(bpy)_2]^+$ (Figure S4a–c, Supporting Information). The metrical parameters involving intramolecular π–π and CH–π interactions as well as nonbonded metal–metal distances of all the compounds under discussion are summarized in Table 3.

Table 3 indicates that the distances between the two π–π interacting pyridine rings and the two metal centers in **1a**, **3a**, and **5a** are correlated and they decrease in the order **1a** (Ru^{II} Ru^{II}) > **5a** (Os^{II} Ru^{II}) > **3a** (Os^{II} Os^{II}). In $[(bpy)_2$-$M^{II}(pzdc)M'^{II}(bpy)_2](ClO_4)\cdot H_2O$ complexes, the π–π distances are shorter and both π–π and metal–metal distances remain practically unchanged with the change in the metal centers across the series.

^{1}H NMR Spectra

The ^{1}H NMR spectra of the homochiral and heterochiral $[(ppy)_2Ru^{II}(H_2pzbzim)Ru^{II}(ppy)_2]^{3+}$ and $[(ppy)_2Ru^{II}$-$(pzbzim)Ru^{II}(ppy)_2]^+$ complexes, including $\mathbf{1a}^{3+}$, $\mathbf{1b}^{3+}$, $\mathbf{2a}^+$, and $\mathbf{2b}^+$, have been reported earlier.[30a] In Figure 3, the spectra of $[(bpy)_2Os^{II}(H_2pzbzim)Os^{II}(bpy)_2]^{3+}$ in $(CD_3)_2SO$ before and after separation of the *meso* (ΛΔ $\mathbf{3a}^{3+}$) and *rac* (ΛΛ/ΔΔ $\mathbf{3b}^{3+}$) forms are shown. The assignments made for the observed chemical shifts, according to the numbering scheme (shown in Scheme 2), are listed in Table 4.

The spectral assignments of $\mathbf{3a}^{3+}$ and $\mathbf{3b}^{3+}$ have been made with the help of their $\{^1H$–$^1H\}$ COSY spectra (Figure S5, Supporting Information), relative areas of the peaks, and taking into consideration the usual ranges of *J* values for bpy.[36] It may be noted that the H3, H6, H11, and H14 protons are observed as doublets, while the H4,

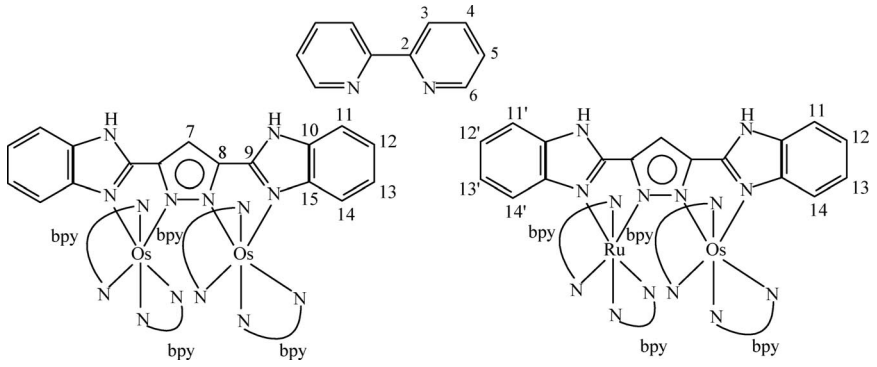

Scheme 2.

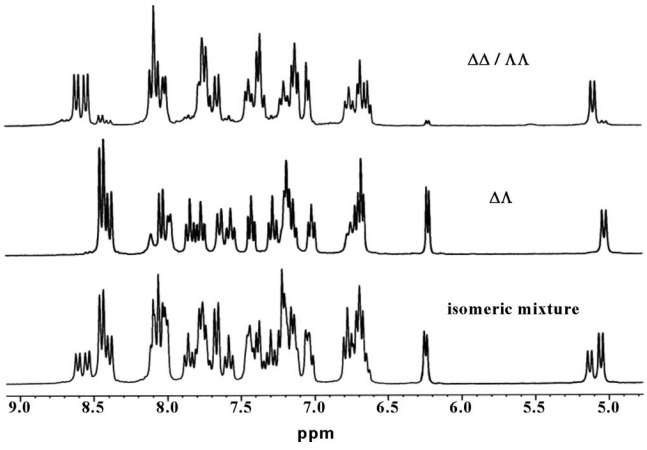

Figure 3. ^{1}H NMR spectra of the diastereoisomers **3a** (ΔΛ) and **3b** (ΔΔ/ΛΛ) of the complex $[(bpy)_2Os(H_2pzbzim)Os(bpy)_2](ClO_4)_3 \cdot 3H_2O$ in $(CD_3)_2SO$.

H5, H12, and H13 protons are observed either as triplets or doublet of doublets. However, due to overlapping of some of these signals their splitting patterns are obscured (Table 4).

The pair of doublets observed at δ = 5.03 and 5.12 ppm and the pair of singlets observed at δ = 14.52 and 14.56 ppm in $\mathbf{3}^{3+}$ have been used as markers for separation of the less-soluble *meso* ($\mathbf{3a}^{3+}$) and the more-soluble *rac* ($\mathbf{3b}^{3+}$) forms. As may be seen in Figure 3, the doublet at δ = 5.03 ppm and the singlet at δ = 14.56 ppm belong to $\mathbf{3a}^{3+}$, while the corresponding signals in $\mathbf{3b}^{3+}$ occur at δ = 5.12 and 14.52 ppm. The signal observed at δ = 5.03 or 5.12 ppm is remarkably upfield-shifted relative to all other resonances, indicating that the proton(s) concerned must be shielded due to the anisotropic ring current effect. As already noted in Figure 1, the phenyl ring protons H2 and H16 of the bridging ligand are very close to the centroids of the pyridyl rings having the N3 and N11 nitrogen atoms.

Table 4. ^{1}H NMR spectroscopic data[a,b] for the *meso* and *rac* diastereoisomers of complexes $[(bpy)_2Os(H_2pzbzim)Os(bpy)_2](ClO_4)_3 \cdot 2H_2O$ (**3**) and $[(bpy)_2Os(pzbzim)Os(bpy)_2](ClO_4) \cdot 2H_2O$ (**4**).

Proton	$[(bpy)_2Os(H_2pzbzim)Os(bpy)_2]^{3+}$ ($\mathbf{3}^{3+}$) $\mathbf{3a}^{3+}$ (*meso* ΛΔ) $\mathbf{3b}^{3+}$ (*rac* ΛΛ/ΔΔ)		$[(bpy)_2Os(pzbzim)Os(bpy)_2]^{+}$ ($\mathbf{4}^{+}$) $\mathbf{4a}^{+}$ (*meso* ΛΔ) $\mathbf{4b}^{+}$ (*rac* ΛΛ/ΔΔ)	
H14	5.03, d (J = 8.3 Hz), 2 H	5.12, d (J = 8.3 Hz), 2 H	4.78, d (J = 8.2 Hz), 2 H	4.91, d (J = 8.1 Hz), 2 H
H13	6.73, t (J = 7.8 Hz), 2 H	6.73, t (J = 7.6 Hz), 2 H	6.28, t (J = 7.6 Hz), 2 H	6.29, t (J = 7.7 Hz), 2 H
H12	7.16, t (J = 7.8 Hz), 2 H	7.20, t (J = 7.8 Hz), 2 H	6.71, t (J = 6.6 Hz), 2 H	6.71, m,[c] 2 H
H11	7.64, d (J = 8.1 Hz), 2 H	7.65, d (J = 8.1 Hz), 2 H	7.37, m,[c] 2 H	7.38, d (J = 8.1 Hz), 2 H
H7	8.09, s, 1 H	8.08, s, 1 H	7.48, s, 1 H	7.44, s, 1 H
H6	7.99, d (J = 5.2 Hz), 2 H	8.01, d (J = 5.6 Hz), 2 H	7.35, m,[c] 2 H	8.10, d (J = 5.6 Hz), 2 H
	7.18, d (J = 5.3 Hz), 2 H	7.12, d (J = 5.4 Hz), 2 H	7.03, d (J = 5.4 Hz), 2 H	7.07, m,[c] 2 H
	6.66, d (J = 5.7 Hz), 2 H	7.04, d (J = 5.5 Hz), 2 H	6.82, d (J = 5.4 Hz), 2 H	6.92, d (J = 5.3 Hz), 2 H
	6.23, d (J = 5.4 Hz), 2 H	6.69, d (J = 5.4 Hz), 2 H	6.22, d (J = 5.3 Hz), 2 H	6.71, m,[c] 2 H
H5	7.43, t (J = 6.4 Hz), 2 H	7.43, t (J = 6.5 Hz), 2 H	7.64, t (J = 6.5 Hz), 2 H	7.32, t (J = 6.6 Hz), 2 H
	7.15, t (J = 6.9 Hz), 2 H	7.35, m,[c] 2 H	7.39, m,[c] 2 H	7.07, m,[c] 2 H
	7.02, t (J = 6.9 Hz), 2 H	7.14, t (J = 6.5 Hz), 2 H	6.88, t (J = 6.6 Hz), 2 H	7.02, t (J = 6.7 Hz), 2 H
	6.70, t (J = 6.9 Hz), 2 H	6.63, m,[c] 2 H	6.64, t (J = 6.6 Hz), 2 H	6.57, t (J = 6.6 Hz), 2 H
H4	7.83, t (J = 7.7 Hz), 2 H	7.65–7.76, m,[c] 4 H	7.69, t (J = 7.8 Hz), 2 H	7.63, t (J = 7.7 Hz), 2 H
	7.77, t (J = 7.6 Hz), 2 H	7.35, m,[c] 2 H	7.40, m,[c] 2 H	7.58–7.48, m,[c] 4 H
	7.56, t (J = 7.7 Hz), 2 H	7.20, t (J = 7.7 Hz), 2 H	7.31, t (J = 7.7 Hz), 2 H	7.27, t (J = 7.8 Hz), 2 H
	7.28, t (J = 7.7 Hz), 2 H		7.17, t (J = 7.8 Hz), 2 H	
H3	8.43, d (J = 8.2 Hz), 4 H	8.60, d (J = 8.2 Hz), 2 H	8.32–8.42, m,[c] 6 H	8.53, d (J = 8.3 Hz), 2 H
	8.37, d (J = 8.2 Hz), 2 H	8.53, d (J = 8.2 Hz), 2 H	8.03, d (J = 8.1 Hz), 2 H	8.47, d (J = 8.3 Hz), 2 H
	8.03, d (J = 8.3 Hz), 2 H	8.09, d (J = 8.3 Hz), 2 H		8.02, d (J = 8.1 Hz), 4 H
		8.06, d (J = 8.3 Hz), 2 H		
NH	14.56, s, 2 H	14.52, s, 2 H		

[a] Chemical shifts in ppm. [b] Proton numbering scheme shown in Scheme 2. [c] Unresolved overlapping signals.

In solution, the two slightly different CH–π distances are averaged and observed as a single resonance in the ^{1}H NMR spectrum. It should be noted that H2 and H16 of Figure 1 are referred to as H14 for homodinuclear systems and H14/H14′ for heterodinuclear systems in Scheme 2. Aside from H2 and H16, other phenyl protons are not sterically oriented for CH–π interaction to experience ring current effect. The most downfield-shifted resonance in **3a**$^{3+}$ (δ =14.56 ppm) or **3b**$^{3+}$ (δ =14.52 ppm) is due to the benzimidazole NH, which is hydrogen bonded to $(CD_3)_2SO$. From the chemical shift values listed in Table 4 it is evident that for all the resonances due to the bridging ligand the *meso* (**3a**$^{3+}$) and *rac* (**3b**$^{3+}$) forms have comparable values, although significant differences in the chemical shifts occur for the bpy protons in the two diastereoisomers due to their disparity in spatial orientations.

In Figure 4, the ^{1}H NMR spectra of the deprotonated diosmium(II) complex $[(bpy)_2Os^{II}(pzbzim)Os^{II}(bpy)_2]^+$ (**4**$^+$), its *meso* (**4a**$^+$), and *rac* (**4b**$^+$) forms are shown.

As compared to **3a**$^{3+}$ and **3b**$^{3+}$, the protons of the bridging ligand in **4a**$^+$ and **4b**$^+$ are even more upfield shifted. For instance, the doublet due to H14 is observed at δ = 4.78 ppm in **4a**$^+$ (δ =5.03 ppm in **3a**$^{3+}$) and at δ = 4.91 ppm in **4b**$^+$ (δ =5.12 ppm in **3b**$^{3+}$). Indeed, the extent to which the H7 and H11–H14 protons are upfield shifted in the two deprotonated diastereoisomers range from 0.22 to 0.64 ppm, with the maximum change observed for the pyrazolate H7 proton (Table 4). Obviously, as the negative charge of the bridging ligand increases from –1 to –3, the electronic charge densities of the ligand hydrogen atoms also increase and they are more shielded. In contrast, the chemical shifts of the bpy protons in **4a**$^+$ and **4b**$^+$ are not significantly different from those of **3a**$^{3+}$ and **3b**$^{3+}$, respectively.

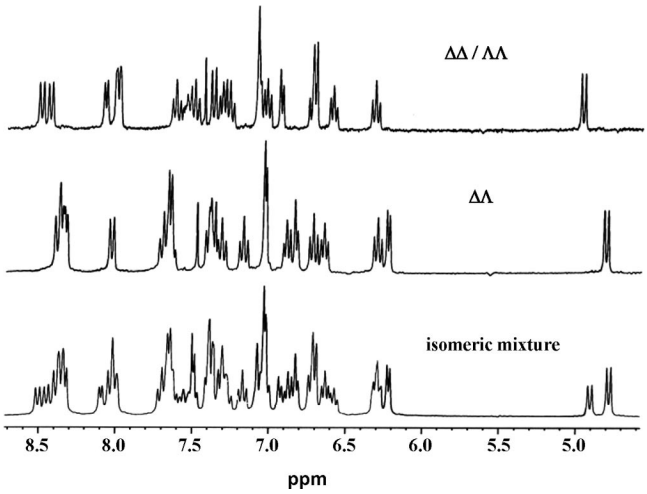

Figure 4. ^{1}H NMR spectra of the diastereoisomers **4a** (ΔΛ) and **4b** (ΔΔ/ΛΛ) of the complex $[(bpy)_2Os(pzbzim)Os(bpy)_2](ClO_4)\cdot 2H_2O$ in $(CD_3)_2SO$.

Table 5. ^{1}H NMR spectroscopic data[a,b] for the heterochiral (ΛΔ/ΔΛ) and homochiral (ΛΛ/ΔΔ) diastereoisomers of complexes $[(bpy)_2Os(H_2pzbzim)Ru(bpy)_2](ClO_4)_3\cdot 4H_2O$ (**5**) and $[(bpy)_2Os(pzbzim)Ru(bpy)_2](ClO_4)\cdot 3H_2O$ (**6**).

Proton	$[(bpy)_2Os(H_2pzbzim)Ru(bpy)_2]^{3+}$ (**5**$^{3+}$)		$[(bpy)_2Os(pzbzim)Ru(bpy)_2]^+$ (**6**$^+$)	
	5a^{3+} (ΛΔ/ΔΛ)	**5b**$^{3+}$ (ΛΛ/ΔΔ)	**6a**$^+$ (ΛΔ/ΔΛ)	**6b**$^+$ (ΛΛ/ΔΔ)
H14/14′	5.02, d (J = 8.3 Hz), 1 H 5.04, d (J = 8.3 Hz), 1 H	5.10, d (J = 8.4 Hz), 1 H 5.15, d (J = 8.4 Hz), 1 H	4.81, d (J = 8.1 Hz), 1 H 4.89, d (J = 8.2 Hz), 1 H	4.90–4.96, m,[c] 2 H
H13/13′	6.75, m,[c] 2 H	6.78–7.07, m,[c] 2 H	6.34–6.40, m,[c] 1 H 6.47, t (J = 7.5 Hz), 1 H	6.30–6.38, m,[c] 2 H
H12/12′	7.10–7.30, m,[c] 2 H	7.10–7.17, m,[c] 2 H	6.63, t (J = 7.8 Hz), 1 H 6.76–6.93, m,[c] 1 H	6.54–6.58, m,[c] 1 H 6.70–6.78, m,[c] 1 H
H11/11′	7.64, d (J = 8.2 Hz), 2 H	7.62–7.68, m,[c] 2 H	7.42, d (J = 8.2 Hz), 2 H	7.36, d (J = 8.3 Hz), 2 H
H7	8.10, s,[c] 1 H	8.10, s,[c] 1 H	7.69, s,[c] 1 H	7.60, s,[c] 1 H
H6	6.26, d (J = 5.3 Hz), 1 H 6.36, d (J = 5.4 Hz), 1 H 7.10–7.30, m,[c] 2 H 7.44, d (J = 5.4 Hz), 2 H 7.57, d (J = 5.3 Hz), 2 H	6.64, d (J = 5.3 Hz), 1 H 6.78–7.08, m,[c] 3 H 7.24, d (J = 5.3 Hz), 4 H	6.24, d (J = 5.3 Hz), 1 H 6.34–6.40, m,[c] 1 H 6.76–6.93, m,[c] 6 H	6.70–6.78, m,[c] 4 H 6.94, d (J = 5.2 Hz), 1 H 7.03–7.09, m,[c] 3 H
H5	6.66, t (J = 6.6 Hz), 2 H 6.82, t (J = 6.5 Hz), 2 H 7.02, t (J = 6.6 Hz), 1 H 7.10–7.30, m,[c] 3 H	6.78–7.07, m,[c] 2 H 7.26–7.48, m,[c] 6 H	7.02–7.13, m,[c] 2 H 7.14–7.24, m,[c] 3 H 7.28–7.42, m,[c] 3 H	7.20–7.32, m,[c] 6 H 7.50–7.65, m,[c] 2 H
H4	7.77, t (J = 7.7 Hz), 2 H 7.85, t (J = 7.8 Hz), 1 H 7.91, t (J = 7.8 Hz), 1 H 7.94–8.04, m,[c] 4 H	7.71–7.79, m,[c] 4 H 7.96–8.05, m,[c] 4 H	7.65–7.71, m,[c] 4 H 7.83, t (J = 7.8 Hz), 1 H 7.90–8.10, m,[c] 3 H	7.50–7.65, m,[c] 4 H 7.96–8.02, m,[c] 4 H
Proton	$[(bpy)_2Os(H_2pzbzim)Ru(bpy)_2]^{3+}$ (**5**$^{3+}$)		$[(bpy)_2Os(pzbzim)Ru(bpy)_2]^+$ (**6**$^+$)	
	5a^{3+} (ΛΔ/ΔΛ)	**5b**$^{3+}$ (ΛΛ/ΔΔ)	**6a**$^+$ (ΛΔ/ΔΛ)	**6b**$^+$ (ΛΛ/ΔΔ)
H3	8.14, m,[c] 2 H 8.36–8.50, m,[c] 6 H	7.96–8.05, m,[c] 4 H 8.52–8.67, m,[c] 4 H	8.01, d (J = 8.1 Hz), 2 H 8.35–8.45, m,[c] 6 H	8.08, d (J = 8.1 Hz), 2 H 8.59, d (J = 8.1 Hz), 6 H
NH	14.38, s, 1 H 14.36, s, 1 H	14.47, s, 1 H 14.53, s, 1 H		

[a] Chemical shifts in ppm. [b] Proton numbering scheme shown in Scheme 2. [c] Unresolved overlapping signals.

Figure 5 shows the ^{1}H NMR spectra of the heterobinuclear complex $[(bpy)_2Os^{II}(H_2pzbzim)Ru^{II}(bpy)_2]^{3+}$ ($\mathbf{5}^{3+}$) before and after separation of the two enantiomeric pairs $\mathbf{5a}^{3+}$ (heterochiral ΛΔ/ΔΛ) and $\mathbf{5b}^{3+}$ (homochiral ΛΛ/ΔΔ). The spectra, especially that of $\mathbf{5}^{3+}$, look complicated, because of the presence of many signals and extensive overlapping. The two benzimidazole units of $H_2pzbzim^-$ in $\mathbf{5}^{3+}$ are no longer magnetically equivalent, and accordingly, two sets of resonances due to the NH, H11–H14, and H11′–H14′ protons (Scheme 2) can be expected to be observed in $\mathbf{5a}^{3+}$ and $\mathbf{5b}^{3+}$. The chemical shifts of $\mathbf{5a}^{3+}$ and $\mathbf{5b}^{3+}$ catalogued in Table 5 have been assigned to a reasonable extent with the help of their {^{1}H–^{1}H} COSY spectra (Figure S6, Supporting Information).

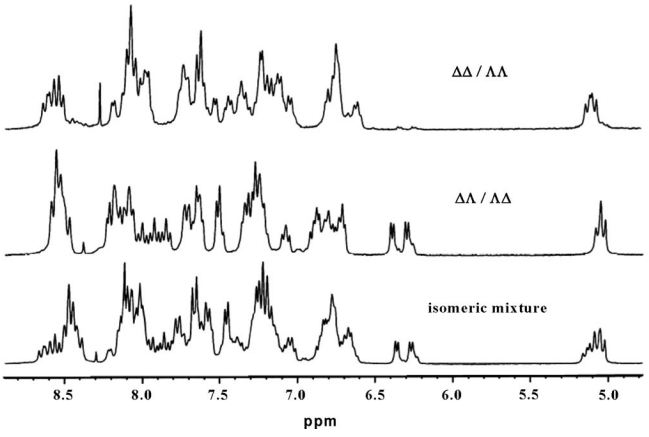

Figure 5. ^{1}H NMR spectra of the diastereoisomers **5a** (ΔΛ/ΛΔ) and **5b** (ΔΔ/ΛΛ) of the complex $[(bpy)_2Os(H_2pzbzim)Ru(bpy)_2](ClO_4)_3{\cdot}4H_2O$ in $(CD_3)_2SO$.

Finally, the ^{1}H NMR spectra of $[(bpy)_2Os^{II}(pzbzim)Ru^{II}(bpy)_2]^+$ ($\mathbf{6}^+$) and its two diastereoisomers $\mathbf{6a}^+$ (ΛΔ/ΔΛ) and $\mathbf{6b}^+$ (ΛΛ/ΔΔ) are shown in Figure S7 (Supporting Information) and the chemical shifts are listed in Table 5. It may be noted that the bridging ligand protons in $\mathbf{6a}^+$ and $\mathbf{6b}^+$ show expected greater shielding of their chemical shifts compared to those of $\mathbf{5a}^{3+}$ and $\mathbf{5b}^{3+}$.

Absorption Spectra

The UV/Vis spectroscopic data for the homochiral and heterochiral diastereoisomers of complexes **1**–**6** are catalogued in Table 6. In the UV region, all the complexes exhibit three bands at ca. 240, 295, and 340 nm due to intraligand π–π* transitions. The visible spectrum of diruthenium(II) complex $\mathbf{1}^{3+}$ displays two MLCT bands at about 435 and 495 nm, while in diosmium(II) complex $\mathbf{3}^{3+}$, these two bands occur at ca. 422 and 502 nm. Complex $\mathbf{3}^{3+}$ exhibits an additional broad band at ca. 700 nm due to Os(dπ) → bpy(π*) triplet transition, which occurs because of strong spin–orbit coupling introduced by osmium(II).[37,38] In heterodinuclear complex $\mathbf{5}^{3+}$, the number of bands observed in the visible region at around 438, 488, 504, and 690 nm are more numerous because of the occurrence of MLCT transitions for both ruthenium(II) and osmium(II). A comparison of the spectroscopic data for homochiral and heterochiral diastereoisomers (Table 6) reveals that for any given complex the difference is quite small. Specifically, the MLCT bands of the homochiral diastereoisomers of all complexes (**1**–**6**) are shifted to higher wavelengths relative to their heterochiral counterparts by ca. 3–5 nm. Similar small spectral differences between the two diastereoisomers in $[(bpy)_2M^{II}(pzdc)M'^{II}(bpy)_2]^+$ complexes have been observed by us.[30d,30f] In the literature, for a number of systems[12a,12b,13c,14d,14e,14l,15d,15e] either no spectral difference between the diastereoisomers or their variation up to 7 nm has been reported. In light of the fact that uncertainty involved in detecting the peak position of an absorption band could be ±2 nm, the spectral difference observed by us may be regarded as nil to nominal.

Substantial spectral redshifts, however, occur when $[(bpy)_2M^{II}(H_2pzbzim)M'^{II}(bpy)_2]^{3+}$ are deprotonated to $[(bpy)_2M^{II}(pzbzim)M'^{II}(bpy)_2]^+$. Thus, each of the MLCT bands of $\mathbf{1}^{3+}$, $\mathbf{3}^{3+}$, and $\mathbf{5}^{3+}$ are shifted to higher wavelengths by about 30 to 35 nm in corresponding deprotonated analogues $\mathbf{2}^+$, $\mathbf{4}^+$, and $\mathbf{6}^+$. The consequences of deprotonation are reduction in the cationic charge by 2 units, augmentation of the electron densities at the metal centers,

Table 6. Absorption spectroscopic data[a] for the homochiral and heterochiral diastereoisomers of complexes **1**–**6**.

Compound	λ_{max} / nm (ε / $M^{-1}cm^{-1}$)	
	Heterochiral (**a** ΛΔ/ΔΛ)	Homochiral (**b** ΛΛ/ΔΔ)
$[(bpy)_2Ru(H_2pzbzim)Ru(bpy)_2]^{3+}$ ($\mathbf{1}^{3+}$)	242 (64200), 294 (87500), 335 (34300), 433 (9070), 492 (12400)	240 (65000), 295 (86000), 336 (33000), 436 (9000), 496 (12100)
$[(bpy)_2Ru(pzbzim)Ru(bpy)_2]^+$ ($\mathbf{2}^+$)	241 (65000), 296 (85000), 325 (38800), 468 (9200), 524 (10800)	240 (64500), 295 (84000), 324 (40000), 472 (9000), 528 (11000)
$[(bpy)_2Os(H_2pzbzim)Os(bpy)_2]^{3+}$ ($\mathbf{3}^{3+}$)	242 (65000), 292 (86000), 344 (34500), 420 (16700), 500 (14200), 700[b] (3500)	240 (65500), 292 (86500), 342 (34000), 425 (16200), 504 (14500), 700[b] (3550)
$[(bpy)_2Os(pzbzim)Os(bpy)_2]^+$ ($\mathbf{4}^+$)	240 (64500), 294 (84000), 345 (33400), 451 (15800), 535 (12300), 800[b] (4100)	240 (64000), 295 (85000), 343 (34000), 455 (15200), 540 (11900), 800[b] (4200)
$[(bpy)_2Os(H_2pzbzim)Ru(bpy)_2]^{3+}$ ($\mathbf{5}^{3+}$)	242 (62000), 292 (85000), 345 (34200), 436 (15800), 486 (14500), 502 (12200), 690 (2150)	240 (63000), 292 (84000), 348 (34800), 440 (15200), 490 (14600), 505 (12500), 690[b] (2200)
$[(bpy)_2Os(pzbzim)Ru(bpy)_2]^+$ ($\mathbf{6}^+$)	242 (63500), 294 (84000), 335 (33500), 466 (14800), 520 (13600), 535 (10800), 800[b] (2600)	242 (63000), 295 (83000), 335 (33000), 470 (15400), 524 (14100), 540 (11200), 800[b] (2700)

[a] In acetonitrile. [b] Broad absorption band.

diminution of the HOMO–LUMO energy gap, and hence lowering of the MLCT band energies. Further to note, the Os(dπ) → bpy(π*) triplet band of $\mathbf{3}^{3+}$ and $\mathbf{5}^{3+}$ is shifted from ca. 700 nm to ca. 800 nm in $\mathbf{4}^{+}$ and $\mathbf{6}^{+}$.

Luminescence Spectra

We have previously reported[30a] the emission spectral characteristics and quantum yields of the diruthenium(II) diastereoisomers of $\mathbf{1a}^{3+}$/$\mathbf{1b}^{3+}$ and $\mathbf{2a}^{+}$/$\mathbf{2b}^{+}$ in acetonitrile (at 300 K) and in 1:4 methanol/ethanol glass (at 77 K) and have observed no significant difference in properties between the *rac* and *meso* forms. When the same study was extended to the complexes of diosmium(II) $\mathbf{3}^{3+}$ and $\mathbf{4}^{+}$ and osmium(II)–ruthenium(II) $\mathbf{5}^{3+}$ and $\mathbf{6}^{+}$, however, for none of these compounds luminescence spectra could be recorded.

Acid Dissociation Constants of Homochiral and Heterochiral Diastereoisomers of $[(bpy)_2M^{II}(H_2pzbzim)M'^{II}(bpy)_2]^{3+}$ ($\mathbf{1}^{3+}$, $\mathbf{3}^{3+}$, $\mathbf{5}^{3+}$)

To assess the influence of chirality and metal centers on the acidities of the benzimidazole moieties of the bridged ligand in $[(bpy)_2M^{II}(H_2pzbzim)M'^{II}(bpy)_2]^{3+}$ complexes, the pK_{ij} values of $\mathbf{1b}^{3+}$, $\mathbf{3a}^{3+}$/$\mathbf{3b}^{3+}$, and $\mathbf{5a}^{3+}$/$\mathbf{5b}^{3+}$ were determined spectrophotometrically in acetonitrile/water (3:2). The pK_{ij} values were determined in the same way as that reported earlier by us[30a] for $\mathbf{1a}^{3+}$. Typical absorption spectral changes for *rac* $[(bpy)_2Os^{II}(H_2pzbzim)Os^{II}(bpy)_2]^{3+}$ ($\mathbf{3b}^{3+}$) and heterochiral $[(bpy)_2Os^{II}(H_2pzbzim)Ru^{II}(bpy)_2]^{3+}$ ($\mathbf{5a}^{3+}$) over the pH range 3.0–12.0 are shown in Figures 6 and 7, respectively.

On close inspection of the changes in the spectral profiles with the variation of pH, the occurrence of two successive reaction equilibria [Equation (1)] become evident. This has been verified by establishing the presence of three complex species in solution by analyzing the spectrophotometric data.[39]

$$\begin{array}{c}[(bpy)_2M(H_2pzbzim)M'(bpy)_2]^{3+} \\ \Updownarrow K_{11} \\ [(bpy)_2M(Hpzbzim)M'(bpy)_2]^{2+} + H^+ \\ \Updownarrow K_{12} \\ [(bpy)_2M(pzbzim)M'(bpy)_2]^{+} + H^+ \end{array} \quad (1)$$

The individual pK_{ij} values were evaluated from the two segments of the spectrophotometric titration data at the two appropriate pH ranges by using Equation (2).

$$pK_{ij} = pH + \log\frac{A - A_0}{A_f - A} \quad (2)$$

where A_0, A_f, and A refer to the absorbances at the initial, final, and intermediate pH values at a given wavelength. The pK_{ij} values thus obtained are given in Table 7.

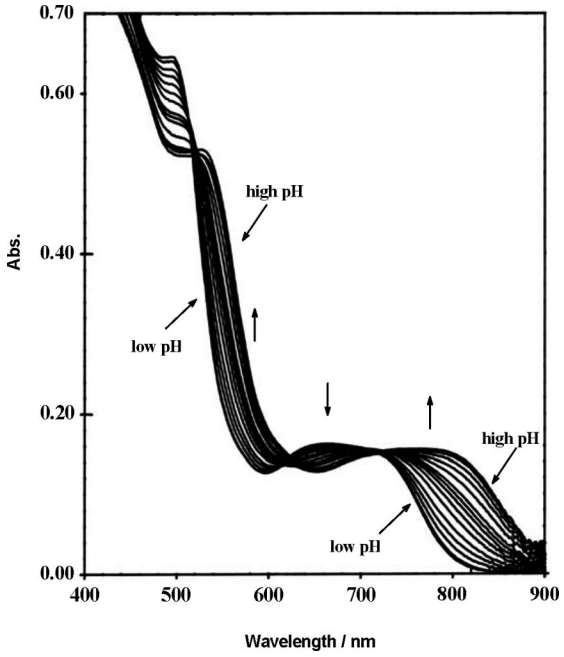

Figure 6. Changes in the absorption spectra of $[(bpy)_2Os(H_2pzbzim)Os(bpy)_2]^{3+}$ ($\mathbf{3b}^{3+}$) with variation of pH (3–12) in acetonitrile/water (3:2).

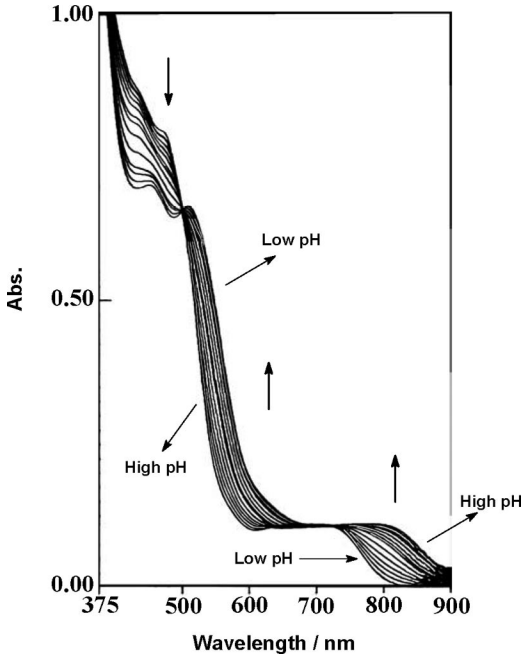

Figure 7. Changes in the absorption spectra of $[(bpy)_2Os(H_2pzbzim)Ru(bpy)_2]^{3+}$ ($\mathbf{5a}^{3+}$) with variation of pH (3–12) in acetonitrile/water (3:2).

The results indicate that the pK_{ij} values of the homochiral diastereoisomers are slightly greater than the heterochiral counterparts, although the difference, in no case, is no more than 0.10. Considering the accuracy of the pK_{ij} values is ±0.05, the influence of chirality on the acid dissociation constants of the benzimidazole moieties of the complexes can be regarded as insignificant.

Table 7. Acid dissociation constants determined spectrophotometrically of homochiral and heterochiral diastereoisomers of $[(bpy)_2M^{II}(H_2pzbzim)M^{II}(bpy)_2]^{3+}$ ($\mathbf{1}^{3+}$, $\mathbf{3}^{3+}$, $\mathbf{5}^{3+}$) in acetonitrile/water (3:2).

	$\mathbf{1a}^{3+}$ (*meso*)[30a]	$\mathbf{1b}^{3+}$ (*rac*)	$\mathbf{3a}^{3+}$ (*meso*)	$\mathbf{3b}^{3+}$ (*rac*)	$\mathbf{5a}^{3+}$ (heterochiral)	$\mathbf{5b}^{3+}$ (homochiral)
pK_{11}	7.95	8.00	7.25	7.30	7.30	7.40
pK_{12}	9.75	9.80	9.40	9.45	9.70	9.80

Concerning the influence of the metal centers on the acidities of the benzimidazole NH protons, both pK_{11} and pK_{12} values of the $Os^{II}Os^{II}$ complex ($\mathbf{3a}^{3+}$/$\mathbf{3b}^{3+}$) are appreciably less than those of the $Ru^{II}Ru^{II}$ complex ($\mathbf{1a}^{3+}$/$\mathbf{1b}^{3+}$). The greater acidity of the diosmium(II) complex relative to that of the diruthenium(II) analogue seems to be related to greater crystal field influence of osmium(II) as well as shorter metal–ligand distances in the diosmium(II) complex. As already noted, in *meso* $Os^{II}Os^{II}$ ($\mathbf{3a}^{3+}$) the average Os–N distances involving the pyrazolate nitrogen atoms (2.125 Å) and the benzimidazole nitrogen atoms (2.081 Å) are shorter than the corresponding distances (2.149 and 2.092 Å) in *meso* $Ru^{II}Ru^{II}$ ($\mathbf{1a}^{3+}$). The shorter Os–N distances of the bridging ligand are likely to induce greater electron withdrawing from the uncoordinated NH residue of the benzimidazole units and thereby increase their acidities.

It is of interest to note that the pK_{11} value of the $Os^{II}Ru^{II}$ complex ($\mathbf{5a}^{3+}$/$\mathbf{5b}^{3+}$) is nearly the same as the pK_{11} value of the $Os^{II}Os^{II}$ complex ($\mathbf{3a}^{3+}$/$\mathbf{3b}^{3+}$), while the pK_{12} value of $\mathbf{5a}^{3+}$/$\mathbf{5b}^{3+}$ is almost identical to the pK_{12} value of the $Ru^{II}Ru^{II}$ complex ($\mathbf{1a}^{3+}$/$\mathbf{1b}^{3+}$). Clearly, in the heterobinuclear $Os^{II}Ru^{II}$ the first acid dissociation of the bridged ligand occurs at the osmium(II) coordinated site.

Redox Properties

The electrochemical behavior of the homochiral and heterochiral diastereoisomers of compounds **1**–**6** was studied in acetonitrile by cyclic, square wave, and differential pulse voltammetric methods. The $E_{1/2}$ values obtained by the three methods agree within ±5 mV. The conventional accuracy of the $E_{1/2}$ values by these techniques, of course, is taken as ±10 mV. The cyclic voltammograms of the heterochiral diastereoisomers $\mathbf{1a}^{3+}$, $\mathbf{3a}^{3+}$, and $\mathbf{5a}^{3+}$ and their corresponding deprotonated species $\mathbf{2a}^{+}$, $\mathbf{4a}^{+}$, and $\mathbf{6a}^{+}$ are shown in Figure 8.

In all the cases, the metal-centered oxidations take place reversibly.[40] The relevant electrochemical data for the homochiral and heterochiral diastereoisomers of compounds **1**–**6** are given in Table 8.

In both the protonated and deprotonated states, the stepwise oxidations of the diruthenium(II) complexes take place at considerably higher positive potentials than the corresponding diosmium(II) complexes. Accordingly, in the heterodinuclear $Os^{II}Ru^{II}$ complexes, the first oxidation takes place for Os^{II} and in the second step Ru^{II} gets oxidized. As

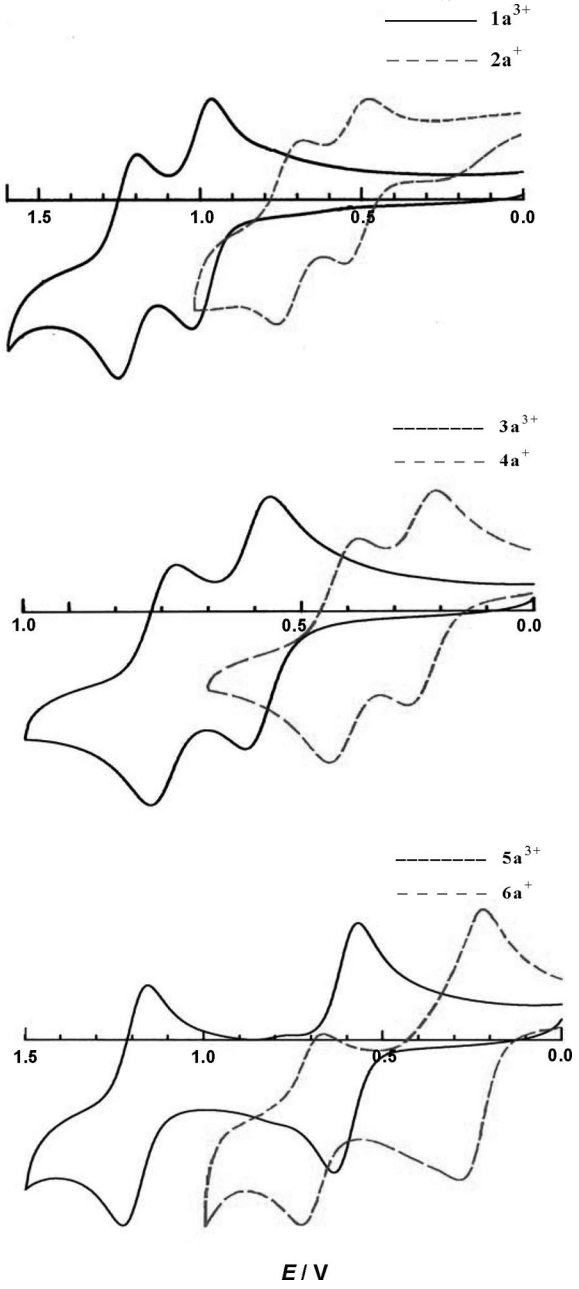

Figure 8. Comparison of cyclic voltammograms of ($\mathbf{1a}^{3+}$, $\mathbf{2a}^{+}$), ($\mathbf{3a}^{3+}$, $\mathbf{4a}^{+}$), and ($\mathbf{5a}^{3+}$, $\mathbf{6a}^{+}$) in acetonitrile.

may be noted in Table 8, in all the cases, both the $E_{1/2}(1)$ and $E_{1/2}(2)$ values of the heterochiral diastereoisomers are slightly greater than the homochiral analogues and the differences between their potentials range from 10 to 25 mV.

As compared to complexes $\mathbf{1}^{3+}$, $\mathbf{3}^{3+}$, and $\mathbf{5}^{3+}$, the redox potentials of corresponding deprotonated complexes $\mathbf{2}^{+}$, $\mathbf{4}^{+}$, and $\mathbf{6}^{+}$ are substantially shifted to less-positive potentials. The lowering of the $E_{1/2}$ values upon deprotonation is correlated with the spectral redshifts that occur for the MLCT bands. For example, in the case of $Ru^{II}Ru^{II}$, conversion of $\mathbf{1}^{3+}$ into $\mathbf{2}^{+}$ is accompanied by lowering of the redox potentials $\Delta E_{1/2}(1)$ and $\Delta E_{1/2}(2)$ by 490 and 510 mV, while diminution of the two MLCT band energies ($\Delta\bar{\nu}$) occur by

Table 8. Electrochemical data[a] for the homochiral and heterochiral diastereoisomers of compounds **1**–**6** in acetonitrile.

Compound/diastereoisomer	Oxidation[b]				Reduction[e]			
	$E_{1/2}(1)$ [mV]	$E_{1/2}(2)$ [mV]	$\Delta E_{1/2}$[c] [mV]	K_c[d]	$E_{1/2}$ [mV]			
$[(bpy)_2Ru^{II}(H_2pzbzim)Ru^{II}(bpy)_2]^{3+}$								
heterochiral (**1a**$^{3+}$)	1020	1230	210	3.57×10^3	–2060	–1880	–1520	–1400
homochiral (**1b**$^{3+}$)	1005	1205	200	2.42×10^3	–2065	–1880	–1510	–1410
$[(bpy)_2Ru^{II}(pzbzim)Ru^{II}(bpy)_2]^{+}$								
heterochiral (**2a**$^{+}$)	530	720	190	1.64×10^3	–2050	–1870	–1505	–1400
homochiral (**2b**$^{+}$)	515	700	185	1.35×10^3	–2045	–1860	–1510	–1400
$[(bpy)_2Os^{II}(H_2pzbzim)Os^{II}(bpy)_2]^{3+}$								
heterochiral (**3a**$^{3+}$)	610	805	195	1.99×10^3	–2070	–1870	–1500	–1400
homochiral (**3b**$^{3+}$)	595	785	190	1.64×10^3	–2075	–1870	–1510	–1410
$[(bpy)_2Os^{II}(pzbzim)Os^{II}(bpy)_2]^{+}$								
heterochiral (**4a**$^{+}$)	250	430	180	1.11×10^3	–2050	–1850	–1490	–1410
homochiral (**4b**$^{+}$)	235	410	175	0.91×10^3	–2060	–1855	–1480	–1410
$[(bpy)_2Os^{II}(H_2pzbzim)Ru^{II}(bpy)_2]^{3+}$								
heterochiral (**5a**$^{3+}$)	610	1210	600		–2040	–1870	–1510	–1420
homochiral (**5b**$^{3+}$)	600	1190	590		–2045	–1865	–1500	–1420
$[(bpy)_2Os^{II}(pzbzim)Ru^{II}(bpy)_2]^{+}$								
heterochiral (**6a**$^{+}$)	255	710	455		–2030	–1865	–1515	–1410
homochiral (**6b**$^{+}$)	245	690	445		–2035	–1860	–1500	–1400

[a] All potentials are referenced against the Ag/AgCl electrode with $E_{1/2}$ = 0.370(5) mV for Fc/Fc$^+$. [b] All metal-centered oxidation processes fulfil the criteria of reversibility. [c] $\Delta E_{1/2} = E_{1/2}(2) - E_{1/2}(1)$. [d] At 298 K. [e] The potentials reported are the values obtained from SWV.

about 1740 and 1230 cm^{-1}. Similarly, for $Os^{II}Os^{II}$ deprotonation of **3**$^{3+}$ to **4**$^{+}$ leads to lowering of the redox potentials by 360 mV [$\Delta E_{1/2}(1)$] and 375 mV [$\Delta E_{1/2}(2)$] and diminution of the MLCT band energies ($\Delta\bar{\nu}$) by ca. 1550 and 1330 cm^{-1}.

It is relevant to compare the equilibrium constant K_c for the comproportionation reaction [Equation (3)] for the diruthenium and diosmium complexes. The value of K_c at 298 K is evaluated by using Equation (4).

$$M^{II}M^{II} + M^{III}M^{III} \overset{K_c}{\rightleftharpoons} 2M^{II}M^{III} \quad (3)$$

$$K_c = 10^{16.92[E_{1/2}(2) - E_{1/2}(1)]} = 10^{16.92\Delta E_{1/2}(V)} \quad (4)$$

While K_c gives a measure of the stability of the mixed-valence $M^{II}M^{III}$ species in equilibrium with the isovalent $M^{II}M^{II}$ and $M^{III}M^{III}$ species, it also indicates the extent of metal–metal interaction in the mixed-valence state. The magnitude of K_c depends upon several factors such as statistical, electrostatic, and inductive effects as well as on the parameter H_{ab} involving donor–acceptor electronic coupling matrix element of the mixed-valence state.[16,22–24] When there is no interaction between the two redox states (class I system), the value of K_c is equal to 4 due to statistical effect only. On the other hand, a value of K_c as high as 2×10^{24} has been reported for a fully valence-delocalized (class III) system.[41] However, for a large number of diruthenium(II) and diosmium(II) complexes the values of K_c have been found to range between 10^2 and 10^8.[22–24] Importantly, several studies have pointed out that specifying mixed-valence systems in the Robin and Day classification scheme[42] on the basis of their K_c values alone may lead to wrong information.[19,43–47]

The values of $\Delta E_{1/2}$ and K_c listed in Table 8 indicate that these values are marginally greater for the heterochiral diastereoisomers than the homochiral analogues. Again, as compared to $[(bpy)_2M^{II}(pzbzim)M^{II}(bpy)_2]^{+}$ complexes, the K_c values of the corresponding $[(bpy)_2M^{II}(H_2pzbzim)M^{II}(bpy)_2]^{3+}$ complexes are greater. Further, the K_c values of the diruthenium(II) complexes are greater than their diosmium(II) analogues. Table 8 shows that for all the cases considered above the highest and lowest values of K_c lie within the narrow range 3.6×10^3 to 0.9×10^3.

The electrochemical data pertaining to reduction of compounds **1**–**6** up to –2.2 V are also included in Table 8. In all the cases, four one-electron reduction processes are observed. However, the first two electron-transfer processes occurring between –1.40 and –1.52 V tend to be overlapped. In the reduction processes, electrons are consecutively transferred to the π-LUMO of the bpy ligands, leading to the generation of metal-coordinated $bpy^{\cdot-}$ species.

Proton-Coupled Electron-Transfer Reactions

To obtain a comprehensive picture encompassing the acid dissociation constants (pK_{ij}), redox potentials [$E_{1/2}(n)$], and bond dissociation free energies ($\Delta G°$) of the complex species that are involved during stepwise proton dissociation of the bridged ligand ($H_2pzbzim^- \rightarrow Hpzbzim^{2-} \rightarrow pzbzim^{3-}$) and oxidation of the metal centers ($M^{II}M^{II} \rightarrow M^{II}M^{III} \rightarrow M^{III}M^{III}$), proton-coupled electron-transfer reactions of the $[(bpy)_2M^{II}(H_2pzbzim)M'^{II}(bpy)_2]^{3+}$ complexes were studied. We previously reported[30a] the $E_{1/2}(1)$ and $E_{1/2}(2)$ vs. pH profiles for *rac* $Ru^{II}Ru^{II}$ (**1b**) in acetonitrile/water (3:2) over the pH range 1–12. Similar measurements have now been carried out for *rac* $Os^{II}Os^{II}$ (**3b**) and

homochiral $Os^{II}Ru^{II}$ (**5b**), and the observations made for the three systems are considered together. The equilibria involved in the proton-coupled electron-transfer reactions[25,26] are outlined in Scheme 3.

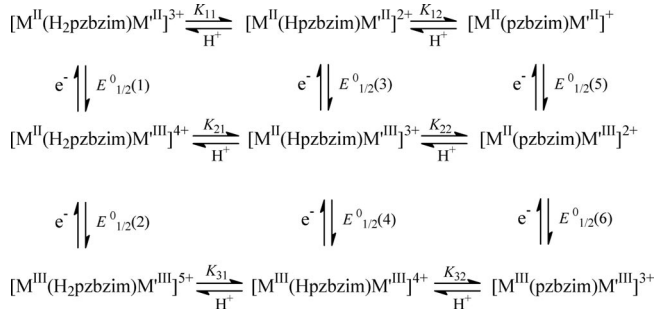

Scheme 3.

In the Scheme 3, $E°_{1/2}(1)$, $E°_{1/2}(3)$, and $E°_{1/2}(5)$ refer to the standard redox potentials for the $M^{II}M^{II}/M^{II}M^{III}$ couple of the complexes, whose bridged ligands are diprotonated ($H_2pzbzim^-$), monoprotonated ($Hpzbzim^{2-}$), and deprotonated ($pzbzim^{3-}$), respectively. Similarly, $E°_{1/2}(2)$, $E°_{1/2}(4)$, and $E°_{1/2}(6)$ are the standard redox potentials for the redox couple $M^{II}M^{III}/M^{III}M^{III}$ of complexes having $H_2pzbzim^-$, $Hpzbzim^{2-}$, and $pzbzim^{3-}$, respectively as the bridged ligand.

The plots of experimental $E_{1/2}(1)$ and $E_{1/2}(2)$ values against pH (1–12) for compounds **3b** and **5b** are shown in Figures 9 and 10, respectively. In the low pH range, where the $E_{1/2}(1)$ and $E_{1/2}(2)$ values remain invariant, the values of $E°_{1/2}(1)$ and $E°_{1/2}(2)$ can be obtained, while the pH-independent $E_{1/2}(1)$ and $E_{1/2}(2)$ values in the high pH region provide the values of $E°_{1/2}(5)$ and $E°_{1/2}(6)$, respectively. Figures 9 and 10 show that in the intermediate pH range, the slopes of $E_{1/2}$ vs. pH plots in all the cases are close to –60 mV/pH unit. This indicates that two successive reaction equilibria, each involving $1H^+/1e^-$ transfer processes have merged together.

The relations between the measured $E_{1/2}(1)$ and $E_{1/2}(2)$ values (at 298 K) and the acid dissociation constants K_{ij} of the complex species are given by Equations (5) and (6).

$$E_{1/2}(1) = E^0{}_{1/2}(1) + 0.059 \log\frac{[H^+]^2 + K_{11}[H^+] + K_{11}K_{12}}{[H^+]^2 + K_{21}[H^+] + K_{21}K_{22}} \quad (5)$$

$$E_{1/2}(2) = E^0{}_{1/2}(2) + 0.059 \log\frac{[H^+]^2 + K_{21}[H^+] + K_{21}K_{22}}{[H^+]^2 + K_{31}[H^+] + K_{31}K_{32}} \quad (6)$$

Nonlinear least-squares analysis of the experimental data provided the best-fit curves, as shown in Figures 9 and 10 by the solid lines. The pK_{ij} and $E°_{1/2}(n)$ values, thus obtained, are given in Table 9 for **3b** (OsOs) and **5b** (OsRu) along with the previously reported[30a] values for **1b** (RuRu).

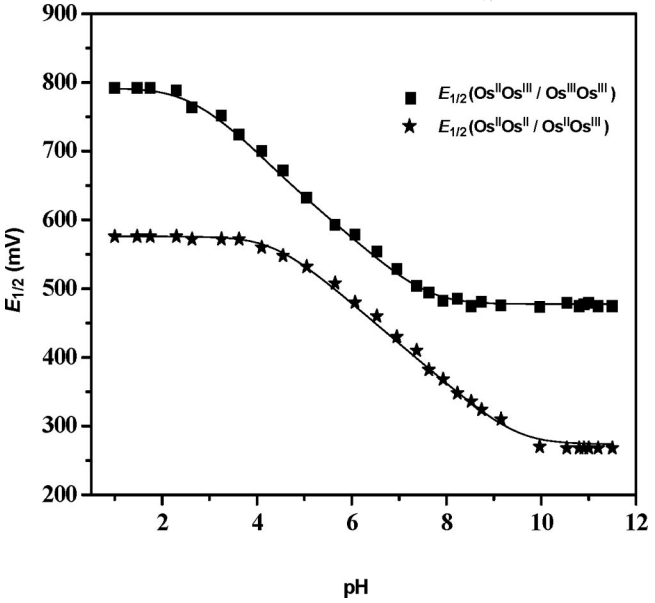

Figure 9. $E_{1/2}$ vs. pH plots for the complex $[(bpy)_2Os(H_2pzbzim)Os(bpy)_2]^{3+}$ ($\mathbf{3}^{3+}$) in acetonitrile/water (3:2). Experimental $E_{1/2}(1)$ and $E_{1/2}(2)$ values are shown as filled squares and stars, respectively, and the solid lines represent the best-fit theoretical curves.

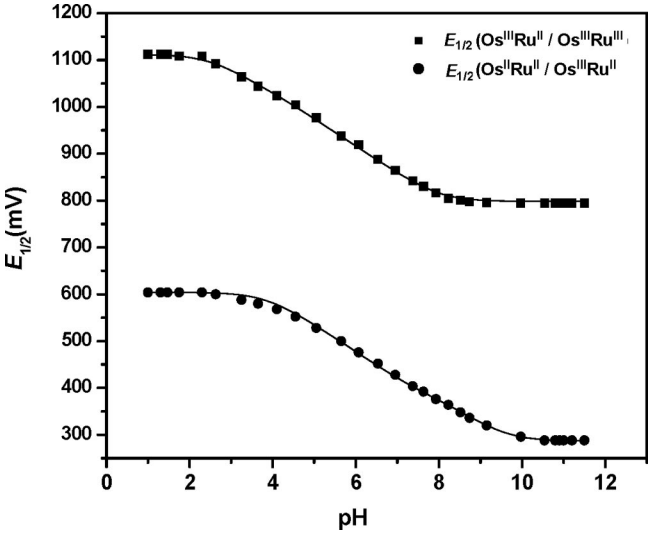

Figure 10. $E_{1/2}$ vs. pH plots for the complex $[(bpy)_2Os(H_2pzbzim)Ru(bpy)_2]^{3+}$ ($\mathbf{5}^{3+}$) in acetonitrile/water (3:2). Experimental $E_{1/2}(1)$ and $E_{1/2}(2)$ values are shown as filled squares and circles, respectively, and the solid lines represent the best-fit theoretical curves.

The results indicate that the pK_{ij} values decrease in the order $pK_{11} > pK_{21} > pK_{31}$ and $pK_{12} > pK_{22} > pK_{32}$. That is, the acidity of the benzimidazole NH protons increase progressively with the increase in the oxidation states of the metal centers ($M^{II}M^{II} \rightarrow M^{II}M^{III} \rightarrow M^{III}M^{III}$). The pK_{ij} values of **3b** (OsOs) are generally lower compared to the corresponding values of **1b** (RuRu). However, the reported low pK_{21} and pK_{32} values for **1b**[30a] are suspect. It may be noted that the pK_{11} and pK_{12} values of the three compounds obtained by the spectrophotometric method compare reasonably well with the values obtained by the elec-

Table 9. Acid dissociation constants [pK_{ij}] and standard redox potentials [$E°_{1/2}(n)$][a] of $M^{II}M^{II}$, $M^{II}M^{III}$, $M^{III}M^{III}$ complex species of homochiral diastereoisomers **1b**, **3b**, and **5b** in acetonitrile/water (3:2).

Compound	pK_{11}	pK_{12}	pK_{21}	pK_{22}	pK_{31}	pK_{32}	$E°_{1/2}(1)$	$E°_{1/2}(2)$	$E°_{1/2}(3)$	$E°_{1/2}(4)$	$E°_{1/2}(5)$	$E°_{1/2}(6)$
1b (RuRu)[b]	7.7 8.00[c]	9.8 9.80[c]	3.5	8.6	1.4	3.7	0.98	1.18	0.73	0.84	0.60	0.78
3b (OsOs)	7.1 7.30[c]	9.2 9.40[c]	4.0	7.3	1.0	4.8	0.58	0.79	0.40	0.60	0.28	0.46
5b (OsRu)	7.3 7.40[c]	9.7 9.80[c]	4.0	8.0	1.0	5.9	0.60	1.11	0.40	0.91	0.30	0.79

[a] $E°_{1/2}(n)$ values in V. [b] Values taken form ref.[30a] [c] Values obtained by spectrophotometric measurements.

trochemical method. The values obtained by the spectrophotometric method are, of course, more accurate.

In order to compare variation of comproportionation constants of **3b** in the three different states of protonation of the bridged ligand, the differences between the $E°_{1/2}(n)$ values of the redox couples $Os^{II}Os^{III}/Os^{III}Os^{III}$ and $Os^{II}Os^{II}/Os^{II}Os^{III}$ in each of the stages of deprotonation are considered. Thus, in the diprotonated state (H_2pzbzim$^-$), $E°_{1/2}(2) - E°_{1/2}(1) = 0.21$ V and $K_c = 3.57 \times 10^3$; in the monoprotonated state (Hpzbzim^{2-}), $E°_{1/2}(4) - E°_{1/2}(3) = 0.20$ V and $K_c = 2.42 \times 10^3$; in the deprotonated state (pzbzim^{3-}), $E°_{1/2}(6) - E°_{1/2}(5) = 0.18$ V and $K_c = 1.11 \times 10^3$. Clearly, the comproportionation constant decreases gradually with an increase in the anionic charge of the bridged ligand. As already noted, in pure acetonitrile, the values of K_c for **3b** in the diprotonated and deprotonated states are 1.64×10^3 and 0.91×10^3, respectively. The dependence of K_c on the composition and dielectric constant of the solvent is therefore evident.

In the case of **1b**, $E°_{1/2}(2) - E°_{1/2}(1) = 0.20$ V and $K_c = 2.42 \times 10^3$; $E°_{1/2}(6) - E°_{1/2}(5) = 0.18$ V and $K_c = 1.11 \times 10^3$. These values are consistent with the trend observed for **3b** and also are in agreement with the K_c values obtained in acetonitrile. However, the difference $E°_{1/2}(4) - E°_{1/2}(3) = 0.11$ V in the monoprotonated state is too low and seems to be inconsistent with the observed trend. It appears that some of the reported $E°_{1/2}(n)$ and pK_{ij} values of **1b**[30a] are less reliable.

In proton-coupled, electron-transfer processes, hydrogen atom transfer reactions[48] represent one particular type where a hydrogen atom ($H^{\cdot} \leftarrow H^+ + e^-$) concertedly transfers from one species to another in a single step. Metal-mediated hydrogen atom transfer reactions invoke a change in the redox state of the metal center with a concurrent change in the protonation state of the ligand, and these are illustrated by Scheme 4, whose diagonal represents hydrogen atom transfer.[49]

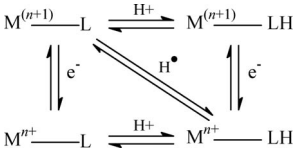

Scheme 4.

In Scheme 4, where horizontal arrows depict pK_{ij} values and vertical arrows show redox potential, $E°_{1/2}(n)$ has been applied to estimate the bond dissociation free energy $\Delta G°$ at 298 K for hydrogen atom transfer by using Equation (7).[49]

$$\Delta G° = [1.37pK_{ij} + 23.1E°_{1/2}(n) + 54.9] \text{ kcal mol}^{-1} \quad (7)$$

The last term in Equation (7) is the free energy value of $H^+ + e^- \rightarrow H^{\cdot}$ in acetonitrile. Although in this work proton-coupled, electron-transfer reactions have been carried out in acetonitrile/water (3:2), the same free energy value (54.9 kcal mol^{-1}) has been used to compare the relative changes of $\Delta G°$ values. Since the total enthalpy change in the thermochemical cycle of the square scheme is zero, it is obvious that the $\Delta G°$ values calculated for the diagonal arrows in the forward and backward directions should be equal. Using the electrochemical data given in Table 9, the $\Delta G°$ values evaluated for each of the square schemes of **3b** (OsOs) in the forward and reverse directions are shown schematically in Figure 11.

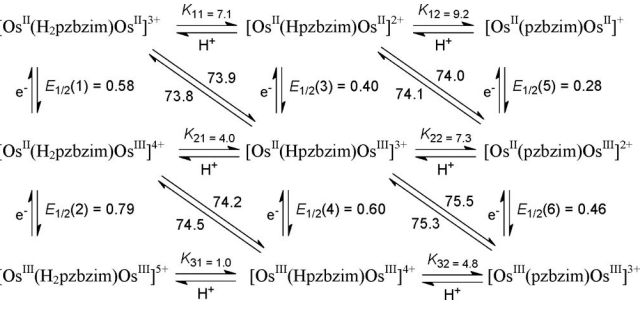

Figure 11. Square scheme of **3b**. Diagonal arrows indicate N–H bond dissociation free energies in kcal mol^{-1}.

Similar representations for **5b** (OsRu) and **1b** (RuRu) are shown in Figures S8 and S9 (Supporting Information), respectively. It may be noted that the average value for the benzimidazole N–H bond dissociation energy for **3b** is 74.6 ± 0.8 kcal mol^{-1}, while in the case of **5b** two sets of average values for $\Delta G°$, 74.6 ± 0.5 and 82.8 ± 1.2 kcal mol^{-1}, have been obtained. On the other hand, the average $\Delta G°$ value for **1b** (RuRu) is 83.0 ± 1.0 kcal mol^{-1}. Clearly, it is more difficult to dissociate the N–H bond in **1b** (RuRu) than in **3b** (OsOs) and an extra energy of ca. 8.2 kcal mol^{-1} is required for **1b** over that of **3b**. Thus, it is relatively more difficult to oxidize the diruthenium complex species, and their pK_{ij} values are also greater than the corresponding diosmium complex species.

Spectroelectrochemistry

Spectroelectrochemical studies were carried out for heterochiral diastereoisomers **1a** ($Ru^{II}Ru^{II}$), **3a** ($Os^{II}Os^{II}$), and **5a** ($Os^{II}Ru^{II}$) in acetonitrile at –25 °C over the spectral range 400 to 1100 nm. To avoid the possibility of thermal degradation of the electrogenerated species, measurements were carried out at low temperature.

Figure 1a shows the spectral changes that occur during one-electron oxidation of $Ru^{II}Ru^{II}$ to $Ru^{II}Ru^{III}$. The MLCT bands of $Ru^{II}Ru^{II}$ at 490 and 432 nm are blueshifted to some extent with lowering of their intensities along with growth of two new bands between 600 and 1100 nm.

All the absorption curves pass through two isosbestic points at 425 and 565 nm. Deconvolution of the spectral feature between 600 and 1100 (Figure 12a, inset) gives rise to two peaks at 695 nm ($\tilde{\nu}$ = 14410 cm^{-1}, ε = 1325 $M^{-1}cm^{-1}$) and 910 nm ($\tilde{\nu}$ = 10960 cm^{-1}, ε = 820 $M^{-1}cm^{-1}$). The band at 695 nm seems to be due to H_2pzbzim → Ru^{III} LMCT transition, while the higher wavelength band is probably due to intervalence charge transfer (IVCT) transition (see later). Further oxidation of $Ru^{II}Ru^{III}$ to $Ru^{III}Ru^{III}$ leads to rapid loss of intensities of the absorption features at 420–470 nm, augmentation of intensity of the band at 695 nm accompanied by blueshift, disappearance of the peak at 910 nm, and growth of a new band with its peak above 1100 nm (Figure 12b). In the process, all the absorption curves pass through three isosbestic points at 540, 810, and 975 nm. The fully generated $Ru^{III}Ru^{III}$ species exhibits LMCT band with its peak at 670 nm (ε = 2250 $M^{-1}cm^{-1}$) and a weak absorption above 1100 nm, presumably due to spin-forbidden dπ–dπ transition. The disappearance of the band at 910 nm of $Ru^{II}Ru^{III}$ on oxidation to $Ru^{III}Ru^{III}$ is noteworthy and provides support to its assignment as the IVCT band.

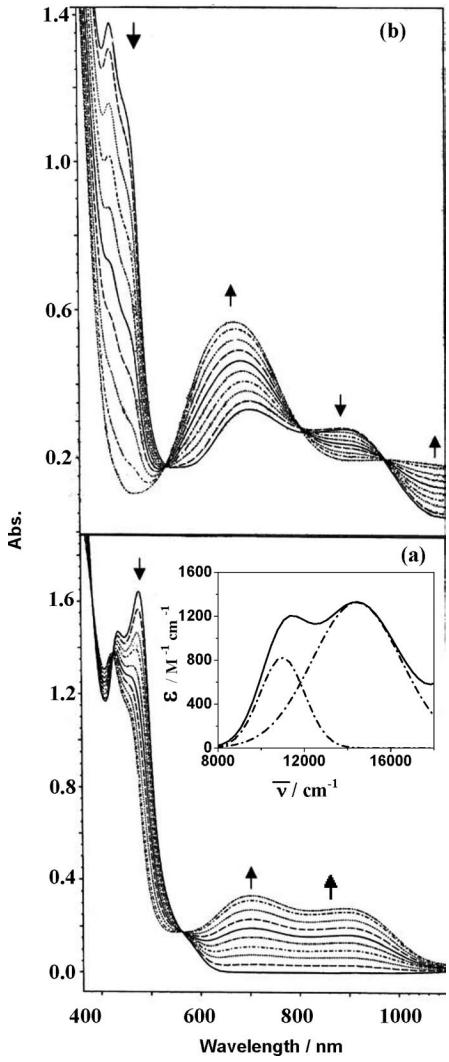

Figure 12. Spectroelectrochemical changes during the oxidation of $[(bpy)_2Ru(H_2pzbzim)Ru(bpy)_2]^{3+}$ ($\mathbf{1}^{3+}$) in acetonitrile. The changes involve $Ru^{II}Ru^{II}$ → $Ru^{II}Ru^{III}$ (a) and $Ru^{II}Ru^{III}$ → $Ru^{III}Ru^{III}$ (b). The IVCT band obtained from spectral deconvolution is shown in inset (a).

The spectrochemical behavior of **5a** ($Os^{II}Ru^{II}$) is shown in Figure S9 (Supporting Information). The transformation $Os^{II}Ru^{II}$ → $Os^{III}Ru^{II}$ is accompanied by diminution of intensities of ^{1}MLCT bands (400–500 nm) and replacement of ^{3}MLCT bands (600–800 nm) by a LMCT band at 650 nm (Figure S10a, Supporting Information). Further oxidation of $Os^{III}Ru^{II}$ to $Os^{III}Ru^{III}$ leads to the disappearance of the ^{1}MLCT bands (400–500 nm) and augmentation of intensity and splitting of the LMCT band at ca. 650 nm into two components with peaks at about 570 and 750 nm (Figure S10b, Supporting Information). The two LMCT bands in $Os^{III}Ru^{III}$ seem to be due to H_2pzbzim → Os^{III} (ca. 570 nm) and $H_2pzbzim^-$ → Ru^{III} (ca. 750 nm) transitions.

In the case of **3b**, the transformation $Os^{II}Os^{II}$ → $Os^{II}Os^{III}$ leads to depletion of intensities of the bands at 450–510 nm (^{1}MLCT). The band at ca. 700 nm due to ^{3}MLCT transition is replaced by a LMCT band with its peak at 650 nm. Importantly, no IVCT band for $Os^{II}Os^{III}$ could be located within 1100 nm.

Because of considering the band observed at λ_{max} = 910 nm in $Ru^{II}Ru^{III}$ as due to IVCT transition, it has been analyzed to obtain more information. In the classical two-state limit for weakly coupled mixed-valence systems,[50] the electronic coupling matrix element H_{ab} is calculated form Gaussian-shaped IVCT band by using Equation (8).[17,50]

$$H_{ab} = \frac{2.06 \times 10^{-2} \left(\bar{\nu}_{max} \varepsilon_{max} \Delta\bar{\nu}_{1/2}\right)^{1/2}}{r_{ab}} \quad (8)$$

In Equation (8), $\Delta\bar{\nu}_{1/2}$ is the observed bandwidth at half-height and r_{ab} is the electron-transfer distance, which is taken as the distance (in Å) between the two interacting metal centers. The predicted bandwidth ($\Delta\bar{\nu}_{1/2}°$) in this model is given by Equation (9).

$$\Delta\bar{\nu}_{1/2}^{o} = [16RT\,\bar{\nu}_{max}\,\ln 2]^{1/2} \quad (9)$$

In the present case, $\bar{\nu}_{max}$ = 10960 cm^{-1}, ε_{max} = 820 $M^{-1}cm^{-1}$, $\Delta\bar{\nu}_{1/2}$ = 2350 cm^{-1}, T = 245 K, and considering that the metal–metal distance in the mixed-valence state

is marginally equal to that in **1a**, $r_{ab} \approx 4.717$ Å. Thus, the calculated values of H_{ab} and $\Delta\bar{\nu}_{1/2}°$ are 635 and 4570 cm^{-1}, respectively. However, the observed bandwidth (2350 cm^{-1}) is much narrower than the expected value (4570 cm^{-1}) and the calculated value of H_{ab} (635 cm^{-1}) also appears to be too large for a weakly interacting system. Indeed, in terms of the Robin and Day classification of mixed-valence systems,[42] the IVCT band(s) in a weakly-coupled valence-localized class II system is expected to be broad, weak, and solvent dependent, and the magnitude of $2H_{ab}$ is much less than the Franck–Condon reorganizational energy λ.[17,18,50] On the other hand, in a valence-delocalized class III system, the IVCT band(s) is narrow, strong, and solvent independent with $2H_{ab} > \lambda$. However, between these two limits, the observation of continuous range of properties has led to recognize a class II–III system[16–19] that underscores localized-to-delocalized transition. For a class II–III system, the valence states are structurally discrete but the IVCT band(s) is narrow and solvent dependent with $2H_{ab} \approx \lambda$. A parameter Γ given by Equation (10) has been introduced to further categorize mixed-valence systems.[17,18] According to this, for a weakly coupled class II system $0.1 < \Gamma < 0.5$, for class II–III system $\Gamma \approx 0.5$, and for class III system $\Gamma > 0.5$.

$$\Gamma = 1 - [\Delta\bar{\nu}_{1/2}/\Delta\bar{\nu}_{1/2}°] \quad (10)$$

In the present $Ru^{II}Ru^{II}$ system, the value of $\Gamma = 0.485$ indicates that it is on the threshold of class II–III. However, its attribution to class II–III on the basis of the observation of a lone IVCT band at a relatively high energy is associated with uncertainty. Ideally, for class II–III systems three low-energy, solvent-independent bands are expected,[16] although these bands may be overlapped. The H_{ab} value estimated by assuming the presence of a single IVCT band could be considerably higher than the real value obtained from the lowest energy IVCT band. Indeed, it has been emphasized[16] that a reasonable assessment of ground-state electronic coupling and estimation of H_{ab} is possible when the low-energy component of the IVCT band is observed. The present study is handicapped by 1100 nm as the highest observable cut-off wavelength of the spectroelectrochemistry instrument. Thus, the band observed at $\lambda_{max} = 910$ nm appears to be the highest-energy component of the possible IVCT bands.

Conclusions

One of the major concerns of this study has been to assess the extent of variations that occur in structural, spectroscopic, and physicochemical properties due to the chirality difference in the $Ru^{II}Ru^{II}$, $Os^{II}Os^{II}$, and $Os^{II}Ru^{II}$ complexes $[(bpy)_2M^{II}(H_2pzbzim)M'^{II}(bpy)_2](ClO_4)_3{\cdot}nH_2O$ (**1**, **3**, **5**) and $[(bpy)_2M^{II}(pzbzim)M'^{II}(bpy)_2](ClO_4){\cdot}nH_2O$ (**2**, **4**, **6**). The structures determined for the heterochiral diastereoisomers (**1a**, **3a**, **5a**) have revealed that in all of them two pyridine rings of two bpy ligands are involved in intramolecular nonbonded π–π interactions. In contrast, the structures of the homochiral congeners (**1b**, **3b**, **5b**) could not be determined due to the lack of suitable crystals, while their molecular models have indicated the absence of π–π interactions. Reexamination of the previously determined structures of the homochiral diastereoisomers of $[(bpy)_2M^{II}(pzdc)M'^{II}(bpy)_2](ClO_4){\cdot}H_2O$[30d,30f] and *meso* $[(bpy)_2Ru^{II}(pzbzth)Ru^{II}(bpy)_2](ClO_4)_3{\cdot}H_2O$[30b] have revealed the presence of strong π–π interaction in all cases. Moreover, the structures of corresponding heterochiral diastereoisomers that could not be determined in the absence of suitable crystals and they also seem to be lacking π–π interaction. Therefore, it may be concluded that the occurrence of strong π–π interaction plays an important role in stabilizing crystalline morphologies of those compounds whose structures have been determined. The difference in spatial configurations of the homochiral and heterochiral diastereoisomers of **1**–**6** are prominently featured in their proton NMR spectra. In **1**–**6**, the MLCT bands of the homochiral diastereoisomers have been found to be shifted to higher wavelengths by 3–5 nm relative to the heterochiral analogues. Similarly, the $E_{1/2}(1)$ and $E_{1/2}(2)$ values of heterochiral diastereoisomers are greater by 10–25 mV compared to the homochiral species. Also, the pK_{11} and pK_{12} values of **1b**, **3b**, and **5b** are greater than those of **1a**, **3a**, and **5a** by 0.05 to 0.10 units. However, if the generally accepted error limits for λ_{max} (±2 nm), $E_{1/2}$ (±10 mV), and pK (±0.05) are taken into consideration, the observed differences of the physicochemical parameters between the diastereoisomeric pairs seem to lie within the range of experimental errors. It may be concluded therefore, that the homochiral and heterochiral diastereoisomers really do not show any significant differences in properties.

Chirality aside, the physicochemical parameters of the complex species based on the metal centers, oxidation states, and protonation states of the bridged ligand exhibit certain trends. The large negative shifts in redox potentials and substantial spectral redshifts in the MLCT bands due to deprotonation are found to be energetically correlated. The values of comproportionation constants K_c decrease gradually as the bridged ligand gets deprotonated ($H_2pzbzim^- \rightarrow Hpzbzim^{2-} \rightarrow pzbzim^{3-}$). The pK_{ij} values of the OsOs species in the II·II, II·III, and III·III oxidation states are lower compared to the RuRu analogues. With the increase in the oxidation states of the metal ions the corresponding pK_{ij} values decrease. In consonance with the greater $E_{1/2}$ and pK_{ij} values of **1** compared to **3**, the bond dissociation free energy of the benzimidazole N–H bond in **1** is about 8.2 kcal mol^{-1} greater than that of **3**. The physicochemical characteristics of the OsRu species are tuned by the parameters of the OsOs and RuRu species.

The spectrochemical studies carried out for **1a**, **3a**, and **5a** have shown the gradual replacements of the more intense LMCT bands observed at relatively lower wavelengths by the less intense MLCT bands shifted to higher wavelengths as the oxidation states of the metal centers change from II·II → II·III → III·III. In the case of **1a**, a relatively narrow band of moderate intensity observed at $\lambda_{max} = 910$ nm has been characterized as the highest energy IVCT band of the $Ru^{II}Ru^{III}$ species.

Experimental Section

Materials: Reagent-grade chemicals obtained from commercial sources were used as received. Solvents were purified and dried according to standard methods.[51] The water used for determining equilibrium constants was deionized and distilled in an all-glass apparatus. The supporting electrolyte tetraethyl/tetrabutylammonium perchlorate (TEAP/TBAP) were prepared from the corresponding bromide salts and perchloric acid and triply recrystallized from hot water and dried at 80 °C for 72 h. H_3pzbzim,[52] *cis*-[Ru(bpy)$_2$Cl$_2$]·2H$_2$O,[53] *cis*-[Os(bpy)$_2$Cl$_2$],[54] [(bpy)$_2$Ru(H_3pzbzim)](ClO$_4$)·2H$_2$O,[30c] and [(bpy)$_2$Os(H_3pzbzim)](ClO$_4$)·2H$_2$O[30c] were prepared according to the reported methods. To adjust the pH value of the solutions in the range 1–12, a series of Robinson-Britton buffer solutions were used.[55]

Physical Measurements: C, H, and N analyses were performed with a Perkin–Elmer 2400 II elemental analyzer. ESI-MS in acetonitrile were obtained with a Micromass Qtof mass spectrometer. ^{1}H and ^{1}H–^{1}H COSY NMR spectra were obtained with a Bruker Avance DPX spectrometer at 300 MHz. UV/Vis absorption spectra were recorded with a Perkin–Elmer Lambda 950 spectrometer.

Electrochemical measurements were carried out with a BAS 100B electrochemistry system using a three-electrode assembly comprising, either a platinum or glassy carbon working electrode, platinum auxiliary electrode, and an aqueous Ag/AgCl reference electrode. Cyclic voltammetric (CV) and square wave voltammetric (SWV) measurements were carried out at 25 °C in acetonitrile, in which the concentration of the complexes and supporting electrolyte (TEAP/TBAP) were maintained at 1 mM and 0.1 M, respectively. The reference electrode was separated from the bulk electrolyte by using a salt bridge. The potentials recorded were automatically compensated for *iR* drop in the cell. Under the given experimental conditions, the potential of the ferrocene/ferrocenium couple (ΔE_p = 60 mV) was found to be 370 (±5) mV.

Variable-pH (1–12) electrochemical measurements were carried out with a series of acetonitrile/water (3:2) solutions containing the same amount of complex (ca. 1 mM) and the same volume of appropriate buffer solutions. As the pH meter responded reproducibly to the variation of hydrogen ion concentrations in the above solvent mixture, the "apparent" pH values obtained directly from the meter readings were referred to as pH.

To determine the pK values of the complexes, spectrophotometric titrations were carried out with a similar series of acetonitrile/water (3:2) solutions containing the same amount of the complexes (ca. 1×10^{-5} M) with incremental variation of pH (by about 0.4 unit) in the range 1–12.

Spectroelectrochemical measurements were performed with a system consisting of an EG & G potentiostat/galvanostat 273 A, a Hewlett–Packard HP 8452 A diode array spectrophotometer and an optically transparent thin-layer electrode (OTTLE) cell. The measurements were carried out under an argon atmosphere at –25 °C.

X-ray Crystal Structure Determinations: X-ray diffraction data for suitable crystals of **3a** and **5a** mounted on a glass fiber and coated with perfluoropolyether oil were collected with a Bruker-AXS SMART APEX II diffractometer at 100 K equipped with a CCD detector using graphite-monochromated Mo-K_α radiation (λ = 0.71073 Å). Crystallographic data and details of structure determination are summarized in Table 10. The data were processed with SAINT[56] and absorption corrections were made with SADABS.[56] The structure was solved by direct and Fourier methods and refined by full-matrix least-squares based on F^2 using the WINGX software, which utilizes SHELX-97.[57] For structure solution and refinement the SHELXTL software package[58] was used. Non-hydrogen atoms were refined anisotropically, while the hydrogen atoms were placed with fixed thermal parameters at idealized positions. In the case of **5a**, of the three anionic perchlorate units, one is severely disordered and could be refined only isotropically. Further, in the complex cation both the metal sites are disordered with almost equal occupancy (0.51Ru/0.49Os for M1, 0.49Ru/0.51Os for M2). The electron density maps showed the presence of some unassignable peaks, which were removed by running the program SQUEEZE.[59]

CCDC-743405 (for **3a**) and -743406 (for **5a**) contain the supplementary crystallographic data for this paper. These data can be obtained free of charge from The Cambridge Crystallographic Data Centre via www.ccdc.cam.ac.uk/data_request/cif.

Table 10. Crystallographic data for *meso* (ΛΔ) [(bpy)$_2$Os(H_3pzbzim)Os(bpy)$_2$](ClO$_4$)$_3$·2H$_2$O (**3a**) and heterochiral (ΛΔ/ΔΛ)[(bpy)$_2$Os(H_3pzbzim)Ru(bpy)$_2$](ClO$_4$)$_3$·4H$_2$O (**5a**).

	3a	**5a**
Empirical formula	$C_{57}H_{43}Cl_{2.5}N_{14}O_{12}Os_2$	$C_{57}H_{51}N_{14}Cl_3O_{16}OsRu$
M_r	1585.08	1585.74
T / K	100(2)	100(2)
Crystal size / mm	0.22 × 0.18 × 0.13	0.12 × 0.18 × 0.22
Crystal system	triclinic	monoclinic
Space group	$P\bar{1}$	$P2_1/c$
a / Å	11.7553(4)	11.5671(2)
b / Å	12.7198(5)	41.6372(8)
c / Å	20.2374(7)	12.6012(2)
/ °	98.3470(10)	90
/ °	92.1700(10)	90.1280(1)
g / °	96.3650(10)	90
V_{UC} / Å^3	2971.00(19)	6069(18)
Z	2	4
$\rho_{calcd.}$ / g cm^{-3}	1.772	1.735
μ / mm^{-1}	4.459	2.554
F(000)	1547	3160
θ range / °	1.63–27.47	1.69–27.88
Index ranges	$-15 \le h \le 14$	$-15 \le h \le 15$
	$-16 \le k \le 16$	$0 \le k \le 54$
	$-25 \le l \le 26$	$0 \le l \le 16$
Reflections collected	40931	14498
Indep. refln.	13220	14498
	(R_{int} = 0.0398)	(R_{int} = 0.00)
Data/restraints/param.	13220/0/817	14498/18/810
GOF on F^2	1.052	1.269
R_1 [F>4σ(F)][a]	0.0426	0.0942
R_1 (all data)	0.0599	0.1055
wR_2 [F>4σ(F)][b]	0.1217	0.2209
wR_2 (all data)	0.1293	0.2249

[a] $R_1(F) = [\Sigma||F_o| - |F_c||/\Sigma|F_o|]$. [b] $wR_2(F^2) = [\Sigma w(F_o^2 - F_c^2)^2/\Sigma w(F_o^2)^2]^{1/2}$.

CAUTION! Perchlorate salts used in this study are potentially explosive and therefore should be handled in small amounts with care.

Preparation of the Dinuclear Metal Complexes: All of the complexes were prepared under oxygen- and moisture-free dinitrogen by using standard Schlenk techniques. The preparation and separation of *meso* (**1a**) and (**2a**) and *rac* (**1b**) and (**2b**) forms of [(bpy)$_2$Ru(H_2pzbzim)Ru(bpy)$_2$](ClO$_4$)$_3$·5H$_2$O (**1**) and [(bpy)$_2$Ru(pzbzim)Ru(bpy)$_2$](ClO$_4$)·3H$_2$O (**2**) have been reported earlier.[30a]

[(bpy)$_2$Os(H$_2$pzbzim)Os(bpy)$_2$](ClO$_4$)$_3$·2H$_2$O (3) and Separation of *meso* (3a) and *rac* (3b) Forms: A mixture of *cis*-[Os(bpy)$_2$Cl$_2$] (0.57 g, 1 mmol), H$_3$pzbzim (0.15 g, 0.5 mmol), and triethylamine (0.05 g, 0.5 mmol) in ethanol/water (1:1, 100 mL) was heated under reflux with continuous stirring for 72 h. The solution was filtered, and to the cooled filtrate (ca. 5 °C) was added an aqueous solution (5 mL) of NaClO$_4$·H$_2$O (1 g). After stirring for 10 min, the dark shinning microcrystalline compound that deposited was filtered. The product was recrystallized twice from methanol/water (10:1) containing a few drops of 1 mM HClO$_4$. Yield: 0.58 g (70%). C$_{57}$H$_{43}$Cl$_{2.50}$N$_{14}$O$_{14}$Os$_2$ (1617.08): calcd. C 41.30, H 2.96, N 11.84; found C 41.39, H 3.07, N 12.01. MS (ESI+, CH$_3$CN): *m*/*z* (%) = 660.5 (60) [(bpy)$_2$Os(H$_2$pzbzim)(OH)Os(bpy)$_2$]$^{2+}$, 651.5 (35) [(bpy)$_2$Os(H$_2$pzbzim)Os(bpy)$_2$]$^{2+}$, 440.1 (100) [(bpy)$_2$Os(H$_2$pzbzim)(OH)Os(bpy)$_2$]$^{3+}$, 435.0 (100) [(bpy)$_2$Os(H$_2$pzbzim)Os(bpy)$_2$]$^{3+}$. The ^{1}H NMR spectrum of **3** indicated it to be a mixture (ca. 1:1) of homochiral (ΛΛ/ΔΔ) *rac* and heterochiral (ΛΔ) *meso* diastereoisomers. Their separation was made by fractional crystallization from methanol/acetonitrile (2:1), in which the *meso* form (**3b**) was less soluble than the *racemate* (**3b**). After four cycles of fractionation diastereoisomerically pure products were obtained. For the diastereoisomers **3a** and **3b** the ^{1}H NMR and UV/Vis spectroscopic data are given in Tables 5 and 7, respectively.

[(bpy)$_2$Os(pzbzim)Os(bpy)$_2$](ClO$_4$)·2H$_2$O (4): To a stirred dry methanol solution (20 mL) of **3** (0.17 g, 0.1 mmol) was added a piece of freshly cut sodium metal. A black microcrystalline product that deposited was collected by filtration and washed successively with water, methanol, and diethyl ether. Upon recrystallization from acetonitrile/methanol (1:1), black shining crystals were obtained. Yield: 0.13 g (95%). C$_{57}$H$_{45}$ClN$_{14}$O$_6$Os$_2$ (1437.93): calcd. C 47.57, H 3.13, N 13.63; found C 47.69, H 3.08, N 13.58. The *meso* (**4a**) and *rac* (**4b**) forms were prepared directly from **3a** and **3b**, respectively. For **4a** and **4b** ^{1}H NMR and UV/Vis spectroscopic data are given in Tables 5 and 7, respectively.

[(bpy)$_2$Os(H$_2$pzbzim)Ru(bpy)$_2$](ClO$_4$)$_3$·4H$_2$O (5) and Separation of ΛΔ/ΔΛ(5a) and ΛΛ/ΔΔ (5b) Enantiomeric Pairs: An ethanol solution (150 mL) of *cis*-[Ru(bpy)$_2$Cl$_2$]·2H$_2$O (0.28 g. 0.5 mmol) was treated with AgClO$_4$ (0.21 g, 1 mmol) and after 15 min of stirring, the precipitated AgCl was removed by filtration. To the filtrate was added [(bpy)$_2$Os(H$_3$pzbzim)](ClO$_4$)·2H$_2$O (0.52 g, 0.5 mmol), followed by triethylamine (0.05 g, 0.5 mmol). The mixture was heated under reflux with continuous stirring for 24 h, after which it was filtered hot. The filtrate was concentrated on a rotary evaporator to ca. 50 mL and then cooled to –5 °C for 10 h. The dark microcrystalline product that deposited was collected by filtration and recrystallized from methanol. Yield: 0.64 g (80%). C$_{57}$H$_{51}$Cl$_3$N$_{14}$O$_{16}$OsRu (1585.74): calcd. C 43.15, H 3.22, N 12.37; found C 43.26, H 3.28, N 12.31. MS (ESI+, CH$_3$CN): *m*/*z* (%) = 607.2 (100) [(bpy)$_2$Os(H$_2$pzbzim)Ru(bpy)$_2$]$^{2+}$, 405.1 (80) [(bpy)$_2$Os(H$_2$pzbzim)Ru(bpy)$_2$]$^{3+}$. Compound **5** thus obtained, was found to be a mixture of two diastereoisomers in ca. 1:1 ratio. The less-soluble heterochiral ΛΔ/ΔΛ **(5a)** enantiomeric pair was separated from the more-soluble homochiral ΛΛ/ΔΔ **(5b)** enantiomeric pair by fractional crystallization from methanol/acetonitrile (2:1) six times. For **5a** and **5b** the ^{1}H NMR and UV/Vis spectroscopic data are reported in Tables 6 and 7.

[(bpy)$_2$Os(pzbzim)Ru(bpy)$_2$](ClO$_4$)·3H$_2$O (6): Compound **6** was prepared from **5** in the same way as that described for **4**. Similarly, **5a** and **5b** were converted into **6a** and **6b**. C$_{57}$H$_{47}$ClN$_{14}$O$_7$OsRu (1366.81): calcd. C 50.08, H 3.44, N 14.34; found C 50.28, H 3.36, N 14.40. For **6a** and **6b**, the ^{1}H NMR and UV/Vis spectroscopic data are given in Tables 6 and 7.

Supporting Information (see footnote on the first page of this article): Additional ESI-MS, crystal structures, ^{1}H NMR spectra, proton-coupled, electron-transfer scheme, and spectroelectrochemical changes.

Acknowledgments

K. N. is thankful to the Indian National Science Academy for providing him support as an INSA Senior Scientist. He is also thankful to the Max Planck Society and to Prof. K. Weighardt of Max Planck Institute for Bioinorganic Chemistry, Mülheim for providing support and hospitality during his stint as MPI Guest Scientist. S. D. is grateful to the Council of Scientific & Industrial Research, India for awarding him a research fellowship. Thanks are due to the Department of Science and Technology, Government of India for establishing the National X-ray diffractometer facility at the Department of Inorganic Chemistry, Indian Association for the Cultivation of Science.

[1] a) V. Balzani, A. Juris, M. Venturi, S. Campagna, S. Serroni, *Chem. Rev.* **1996**, *96*, 759–834; b) V. Balzani, S. Campagna, G. Denti, A. Juris, S. Serroni, M. Venturi, *Acc. Chem. Res.* **1998**, *31*, 26–34; c) V. Balzani, P. Ceroni, M. Maestri, C. Saudan, V. Vicinelli, *Top. Curr. Chem.* **2003**, *228*, 159–191; d) V. Balzani, *Photochem. Photobiol. Sci.* **2003**, *2*, 459–476.

[2] J.-P. Collins, P. Gavina, H. Heitz, J.-P. Sauvage, *Eur. J. Inorg. Chem.* **1998**, 1–14.

[3] a) L. De Cola, P. Besler, *Coord. Chem. Rev.* **1998**, *178–180*, 1251–1298; b) A. Beyler, P. Besler, *Coord. Chem. Rev.* **2002**, *230*, 28–38.

[4] a) J. H. Alstrum-Acevedo, M. K. Brennaman, T. J. Meyer, *Inorg. Chem.* **2005**, *44*, 6802–6827; b) Z. Deng, H.-W. Tseng, R. Zong, D. Wang, R. Thummel, *Inorg. Chem.* **2008**, *47*, 1835–1848; c) I. Romero, M. Rodriguez, C. Sens, J. Mola, M. R. Kollipara, L. Francas, E. Mas-Marza, L. Esriche, A. Llobet, *Inorg. Chem.* **2008**, *47*, 1824–1834.

[5] a) S. Baitalik, X.-y. Wang, R. H. Schmehl, *J. Am. Chem. Soc.* **2004**, *126*, 16304–16305; b) A. D. Del Guerzo, S. Leroy, F. Fages, R. H. Schmehl, *Inorg. Chem.* **2002**, *41*, 359–366; c) A. Baba, J. R. Shaw, J. A. Simon, R. P. Thummel, R. H. Schmehl, *Coord. Chem. Rev.* **1998**, *171*, 43–59; d) J. A. Simon, S. L. Curry, R. H. Schmehl, T. R. Schatz, P. Piotrowiak, X. Jin, R. P. Thummel, *J. Am. Chem. Soc.* **1997**, *119*, 11012–11022; e) J. R. Shaw, R. H. Schmehl, *J. Am. Chem. Soc.* **1991**, *113*, 389–394; f) J. R. Shaw, R. T. Webb, R. H. Schmehl, *J. Am. Chem. Soc.* **1990**, *112*, 1117–1123.

[6] G. Giuffrida, S. Campagna, *Coord. Chem. Rev.* **1994**, *135*/*136*, 517–531.

[7] M. D. Ward, *Chem. Soc. Rev.* **1995**, *24*, 121–134.

[8] E. A. Medlycott, G. S. Hanan, *Chem. Soc. Rev.* **2005**, *34*, 133–142.

[9] R. Ziessel, M. Hissler, A. El-ghayoury, A. Harriman, *Coord. Chem. Rev.* **1998**, *178–180*, 1251–1298.

[10] a) R. Hage, J. G. Haasnoot, H. A. Nieuwenhuis, J. Reedijk, D. A. J. De Ridder, J. G. Vos, *J. Am. Chem. Soc.* **1990**, *112*, 9245–9251; b) R. Hage, J. G. Haasnoot, J. Reedijk, R. Wang, J. G. Vos, *Inorg. Chem.* **1991**, *30*, 3263–3269; c) L. De Cola, F. Barigelletti, V. Balzani, R. Hage, J. G. Haasnoot, J. Reedijk, J. G. Vos, *Chem. Phys. Lett.* **1991**, *178*, 491–496; d) J. H. van Diemen, R. Hage, J. G. Haasnoot, H. E. B. Lempers, J. Reedijk, J. G. Vos, L. De Cola, F. Barigelletti, V. Balzani, *Inorg. Chem.* **1992**, *31*, 3518–3522; e) S. Serroni, S. Campagna, G. Denti, T. E. Keyes, J. G. Vos, *Inorg. Chem.* **1996**, *35*, 4513–4518;

f) F. Frehill, J. G. Vos, S. Benrezzak, A. A. Koos, Z. Konya, M. G. Ruther, W. J. Blau, A. Fonseca, J. B. Nagy, L. P. Biro, A. I. Minett, M. in het Panhuis, *J. Am. Chem. Soc.* **2002**, *124*, 13694–13695; g) S. M. Draper, D. J. Gregg, E. R. Schofield, W. R. Browne, M. Duati, J. G. Vos, P. Passaniti, *J. Am. Chem. Soc.* **2004**, *126*, 8694–8701; h) W. R. Browne, N. M. O'Boyle, W. Henry, A. L. Guckian, S. Horn, T. Fett, C. M. O'Connor, M. Duati, L. De Cola, C. G. Coates, K. L. Ronayne, J. J. McGarvey, J. G. Vos, *J. Am. Chem. Soc.* **2005**, *127*, 1229–1241.

[11] a) M. Haga, M. M. Ali, R. Arakawa, *Angew. Chem. Int. Ed. Engl.* **1996**, *35*, 76–78; b) M. Haga, A. L. Bond, *Inorg. Chem.* **1991**, *30*, 475–480; c) T. Ohno, K. Nozaki, M. Haga, *Inorg. Chem.* **1992**, *31*, 548–555; d) K. Nozaki, T. Ohno, M. Haga, *J. Phys. Chem.* **1992**, *96*, 10880–10887; e) M. Haga, T. Ano, T. Ishizaki, K. Kano, K. Nazaki, T. Ohno, *J. Chem. Soc., Dalton Trans.* **1994**, 263–272.

[12] a) W. R. Browne, D. Hesek, J. F. Gallaher, C. M. O'Connor, J. S. Killen, F. Akoi, H. Ishida, Y. Inoue, C. Vallani, J. G. Vos, *Dalton Trans.* **2003**, 2597–2602; b) W. R. Browne, C. M. O'Connor, C. Vallani, J. G. Vos, *Inorg. Chem.* **2001**, *40*, 5461–5464.

[13] a) X. Hua, A. von Zelewsky, *Inorg. Chem.* **1991**, *30*, 3796–3798; b) P. Hayoz, A. von Zelewsky, H. Stoeckli-Evans, *J. Am. Chem. Soc.* **1993**, *115*, 5111–5114; c) X. Hua, A. von Zelewsky, *Inorg. Chem.* **1995**, *34*, 5791–5797; d) U. Knof, A. Von Zelewsky, *Angew. Chem. Int. Ed.* **1999**, *38*, 302–322.

[14] a) F. R. Keene, *Chem. Soc. Rev.* **1998**, *27*, 185–194; b) F. R. Keene, *Coord. Chem. Rev.* **1997**, *166*, 121–159; c) T. J. Rutherford, M. G. Quagliotto, F. R. Keene, *Inorg. Chem.* **1995**, *34*, 3857–3858; d) L. S. Kelso, D. A. Reitsma, F. R. Keene, *Inorg. Chem.* **1996**, *35*, 5144–5153; e) T. J. Rutherford, F. R. Keene, *Inorg. Chem.* **1997**, *36*, 2872–2878; f) T. J. Rutherford, O. Van Gijte, A. Kirsch-De Mesmaeker, F. R. Keene, *Inorg. Chem.* **1997**, *36*, 4465–4474; g) T. J. Rutherford, F. R. Keene, *Inorg. Chem.* **1997**, *36*, 3580–3581; h) J. A. Treadway, P. Chen, T. J. Rutherford, F. R. Keene, T. J. Meyer, *J. Phys. Chem. A* **1997**, *101*, 6824–6826; i) O. Morgan, S. Wang, S.-A. Bae, R. J. Morgan, A. D. Baker, T. C. Strekas, R. Engel, *J. Chem. Soc., Dalton Trans.* **1997**, 3773–3776; j) B. T. Patterson, F. R. Keene, *Inorg. Chem.* **1998**, *37*, 645–650; k) D. M. D'Alessandro, L. S. Kelso, F. R. Keene, *Inorg. Chem.* **2001**, *40*, 6841–6844; l) D. M. D'Alessandro, F. R. Keene, *Chem. Eur. J.* **2005**, *11*, 3679–3688.

[15] a) F. M. MacDonnell, S. Bodige, *Inorg. Chem.* **1996**, *35*, 5758–5759; b) S. Bodige, A. S. Torres, D. J. Maloney, D. Tate, G. Kinsel, A. Walker, F. M. MacDonnell, *J. Am. Chem. Soc.* **1997**, *119*, 10364–10369; c) S. Bodige, M.-J. Kim, F. M. MacDonnell, *Coord. Chem. Rev.* **1999**, *185/186*, 535–549; d) S. Campagna, S. Serroni, S. Bodige, F. M. MacDonnell, *Inorg. Chem.* **1999**, *38*, 692–701; e) M.-J. Kim, F. M. MacDonnell, M. E. Gimon-Kinsel, T. DuBois, N. Asgharian, J. C. Griener, *Angew. Chem. Int. Ed.* **2000**, *39*, 615–619; f) M.-J. Kim, R. Konduri, H. Ye, F. M. MacDonnell, F. Puntoriero, S. Serroni, S. Campagna, T. Holder, G. Kinsel, K. Rajeshwar, *Inorg. Chem.* **2002**, *41*, 2471–2476.

[16] K. D. Demadis, C. M. Hartshorn, T. J. Meyer, *Chem. Rev.* **2001**, *101*, 2655–2686.

[17] a) C. Creutz, M. D. Newton, N. Sutin, *J. Photochem. Photobiol. A: Chem.* **1994**, *82*, 47–59; b) B. S. Brunschwig, C. Creutz, N. Sutin, *Chem. Soc. Rev.* **2002**, *31*, 168–184.

[18] D. M. D'Alessandro, R. F. Keene, *Chem. Soc. Rev.* **2006**, *35*, 424–440.

[19] W. Kaim, G. K. Lahiri, *Angew. Chem. Int. Ed.* **2007**, *46*, 1778–1796.

[20] a) D. M. D'Alessandro, L. S. Kelso, R. F. Keene, *Inorg. Chem.* **2001**, *40*, 6841–6844; b) D. M. D'Alessandro, A. C. Topley, M. S. Davis, R. F. Keene, *Chem. Eur. J.* **2006**, *12*, 4873–4884.

[21] a) A. C. Benniston, A. Harriman, P. Li, C. A. Sams, M. D. Ward, *J. Am. Chem. Soc.* **2004**, *126*, 13630–13631; b) N. Shan, S. J. Vickers, H. Adams, M. D. Ward, J. A. Thomas, *Angew. Chem. Int. Ed.* **2004**, *43*, 3938–3941.

[22] D. E. Richardson, H. Taube, *Coord. Chem. Rev.* **1984**, *60*, 107–129.

[23] C. Creutz, *Prog. Inorg. Chem.* **1983**, *30*, 1.

[24] a) R. J. Crutchley, *Adv. Inorg. Chem.* **1994**, *41*, 273–325; b) C. E. B. Evans, M. L. Naklicki, A. R. Rezvani, C. A. White, V. V. Kondratriev, R. J. Crutchley, *J. Am. Chem. Soc.* **1998**, *120*, 13096–13103.

[25] M. H. V. Huynh, T. J. Meyer, *Chem. Rev.* **2007**, *107*, 5004–5064.

[26] C. Costentin, *Chem. Rev.* **2008**, *108*, 2145–2179.

[27] M. Haga, M. M. Ali, H. Maegawa, K. Nozaki, A. Yoshimura, T. Ohno, *Coord. Chem. Rev.* **1994**, *132*, 99–104.

[28] G. Bergamini, C. Saudan, P. Ceroni, M. Maestri, V. Balzani, M. Gorka, S.-K. Lee, J. Van Heyst, F. Vögtle, *J. Am. Chem. Soc.* **2004**, *126*, 16466–16471.

[29] Y. Cui, H.-J. Mo, J.-C. Chen, Y.-L. Niue, Y.-R. Zhong, K.-C. Zheng, B.-H. Ye, *Inorg. Chem.* **2007**, *46*, 6427–6436.

[30] a) S. Baitalik, U. Flörke, K. Nag, *Inorg. Chem.* **1999**, *38*, 3296–3308; b) S. Baitalik, U. Flörke, K. Nag, *J. Chem. Soc., Dalton Trans.* **1999**, 719–728; c) S. Baitalik, P. Bag, K. Nag, *Polyhedron* **2002**, *21*, 2481; d) S. Baitalik, U. Flörke, K. Nag, *Inorg. Chim. Acta* **2002**, *337*, 439–449; e) S. Baitalik, B. Dutta, K. Nag, *Polyhedron* **2004**, *23*, 913–919; f) S. Baitalik, P. Bag, U. Flörke, K. Nag, *Inorg. Chim. Acta* **2004**, *357*, 699–706.

[31] C. Janiak, *J. Chem. Soc., Dalton Trans.* **2000**, 3885–3896.

[32] S. R. Wilson, J. S. Moore, *Chem. Eur. J.* **1997**, *3*, 765–771.

[33] C. A. Hunter, J. K. M. Sanders, *J. Am. Chem. Soc.* **1990**, *112*, 5525–5555.

[34] M. Nishino, M. Hirota, Y. Umezawa, *The CH/π Interaction: Evidence, Nature and Consequences*, Wiley-VCH, New York, **1998**.

[35] G. R. Desiraju, T. Steiner, *The Weak Hydrogen Bond in Structural Chemistry and Biology*, Oxford Science Publ., Oxford, **1999**.

[36] J. Bolger, A. Gourdon, E. Ishow, J.-P. Launay, *Inorg. Chem.* **1996**, *35*, 2937–2944.

[37] E. M. Kober, J. V. Caspar, B. P. Sullivan, T. J. Meyer, *Inorg. Chem.* **1988**, *27*, 4587–4598.

[38] S. Campagna, G. Denti, S. Serroni, M. Ciano, A. Juris, V. Balzani, *Inorg. Chem.* **1992**, *31*, 2982–2984.

[39] J. S. Coleman, L. P. Varga, S. H. Mastin, *Inorg. Chem.* **1970**, *9*, 1015–1020.

[40] A. J. Fry, W. E. Britton in *Laboratory Techniques in Electroanalytical Chemistry* (Eds.: P. T. Kissinger, W. R. Heineman), Marcel Dekker, New York, **1984**.

[41] A. Woldarezyr, G. A. Doyle, J. P. Maher, J. A. McCleverty, M. D. Ward, *Chem. Commun.* **1997**, 769–770.

[42] M. B. Robin, P. Day, *Adv. Inorg. Chem. Radiochem.* **1968**, *10*, 247.

[43] a) N. Chanda, B. Sarkar, J. Fiedler, W. Kaim, G. K. Lahiri, *Inorg. Chem.* **2004**, *43*, 5128–5133; b) S. Ghumann, B. Sarkar, N. Chanda, M. Sieger, J. Fiedler, W. Kaim, G. K. Lahiri, *Inorg. Chem.* **2006**, *45*, 7955–7961.

[44] S. Chellamma, M. Lieberman, *Inorg. Chem.* **2001**, *40*, 3177–3180.

[45] C. Patoux, J.-P. Launy, M. Beley, S. Chodorowski-Kimmes, J.-P. Collin, S. James, J.-P. Sauvage, *J. Am. Chem. Soc.* **1998**, *120*, 3717–3725.

[46] S. F. Nelsen, *Chem. Eur. J.* **2000**, *6*, 581–588.

[47] J.-P. Launy, *Chem. Soc. Rev.* **2001**, *30*, 386.

[48] J. T. Hynes, J. P. Klinman, H.-H. Limbach, R. L. Schowen (Eds.), *Hydrogen-Transfer Reactions*, Wiley-VCH, Weinheim, Germany, **2007**.

[49] A. Wu, J. Masland, R. D. Swartz, W. Kaminsky, J. M. Mayer, *Inorg. Chem.* **2007**, *46*, 11190–11201.

[50] a) N. S. Hush, *Prog. Inorg. Chem.* **1967**, *8*, 391; b) N. S. Hush, *Electrochim. Acta* **1968**, *13*, 1005; c) N. S. Hush, *Coord. Chem. Rev.* **1985**, *64*, 135–157.

[51] D. D. Perrin, W. L. Armarego, D. R. Perrin, *Purification of Laboratory Chemicals*, 2nd ed., Pergamon, Oxford, **1980**.

[52] H. H. Lee, B. F. Cain, W. A. Denny, J. S. Buckleton, G. R. Clark, *J. Org. Chem.* **1989**, *54*, 428–431.
[53] B. P. Sullivan, T. J. Meyer, *Inorg. Chem.* **1978**, *17*, 3334–3341.
[54] P. A. Lay, A. M. Sargeson, H. Taube, *Inorg. Synth.* **1986**, *24*, 291.
[55] D. D. Perrin, B. Dempsey, *Buffers for pH and Metal Ion Control*, Chapman and Hall, London, **1974**.
[56] *SAINT* (version 6.02), *SADABS* (version 2.03), Bruker AXS Inc., Madison, Wisconsin, **2002**.
[57] G. M. Sheldrick, *SHELXL-97*, *Program for the Refinement of crystal Structures*, University of Göttingen, Göttingen, Germany, **1997**.
[58] *SHELXTL* (version 6.10), Bruker AXS Inc., Madison, Wisconsin, **2002**.
[59] *PLATON*: A. L. Spek, *J. Appl. Crystallogr.* **2003**, *36*, 7–13.
Received: August 28, 2009
Published Online: December 22, 2009

